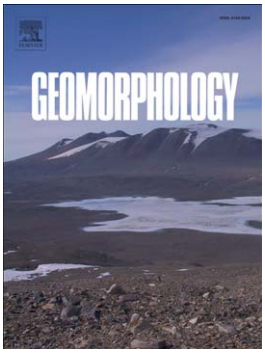

Ground-based multi-view photogrammetry for the monitoring of landslide deformation and erosion

A. Stumpf, J.-P. Malet, P. Allemand, M. Pierrot-Deseilligny, G. Skupinski

PII: S0169-555X(14)00600-X
DOI: doi: 10.1016/j.geomorph.2014.10.039
Reference: GEOMOR 5002

To appear in: *Geomorphology*

Received date: 24 June 2014
Revised date: 21 October 2014
Accepted date: 29 October 2014

Please cite this article as: Stumpf, A., Malet, J.-P., Allemand, P., Pierrot-Deseilligny, M., Skupinski, G., Ground-based multi-view photogrammetry for the monitoring of landslide deformation and erosion, *Geomorphology* (2014), doi: 10.1016/j.geomorph.2014.10.039

Ground-based multi-view photogrammetry for the monitoring of landslide deformation and erosion

Stumpf, A.[a,b,*], Malet, J.-P.[b], Allemand, P.[c], Pierrot-Deseilligny, M.[d], Skupinski, G.[a]

[a] Laboratoire Image, Ville, Environnement, CNRS ERL 7230, Université de Strasbourg, 3 rue de l'Argonne, F-67083, Strasbourg, France. Email: andre.stumpf@unistra.fr

[b] Institut de Physique du Globe de Strasbourg, CNRS UMR 7516, Université de Strasbourg, Ecole et Observatoire des Sciences de la Terre, 5 rue Descartes, F-67084, Strasbourg, France

[c] Laboratoire de Géologie de Lyon, Terre, Planètes, Environnement, CNRS UMR 5276, Université de Lyon, Ecole Normale Supérieure, Bâtiment Géode 2, Campus de la Doua, 2, rue Raphaël Dubois, 69622 Villeurbanne Cedex, France

[d] Ecole Nationale des Sciences Géographiques, 6 et 8 Avenue Blaise Pascal, Cité Descartes, Champs-sur-Marne, Marne la Vallée 77455, France

*Corresponding author. Tel: + 33368850980

E-mail address: andre.stumpf@univ-brest.fr (A. Stumpf)

Highlights

- Open-source photogrammetry permits surface reconstruction in natural terrain with accuracies of a few centimeters to decimeters
- Cloud-to-cloud comparison allows us to detect and quantify surface deformation, erosion and accumulation exceeding 10 cm at 95% confidence
- Landslide volumes and 3D displacement rates are validated through comparison with LiDAR surveys and permanent GPS monitoring

Abstract

Recent advances in multi-view photogrammetry have resulted in a new class of algorithms and software tools for more automated surface reconstruction. These new techniques have a great potential to provide topographic information for geoscience applications at significantly lower costs than classical topographic and laser scanning surveys. Based on open-source libraries for multi-view stereo-photogrammetry and Structure-from-Motion, this study investigates the accuracy that can be obtained from several processing pipelines for the 3D surface reconstruction of landslides and the detection of changes over time. Two different algorithms for point-cloud comparison are tested and the accuracy of the resulting models is assessed against terrestrial and airborne LiDAR point clouds. Change detection over a period of more than two years allows a detailed assessment of the seasonal dynamics of the landslide; the possibility to estimate sediment volumes and 3D displacement are illustrated for the most active parts of the landslide. Algorithm parameters and the image acquisition protocols are found to have important impacts on the quality of the results and are discussed in detail.

Keywords:

Structure-from-motion; Multi-View stereophotogrammetry; Point clouds, Change detection, Landslide; Displacement monitoring

1. Introduction

Digital Elevation Models (DEMs) are indispensable information sources in many geoscientific studies. Modern remote sensing technologies have greatly facilitated their creation and frequent updating for applications in geomorphology, hydrology, geophysics and natural hazards research. Spaceborne observations are valuable sources for obtaining topographic information at global and regional scales (1:100000–1:10000). Measurements at higher spatial resolution and submetre accuracy are required for the investigation at local scales (< 1:10000) where topographic information can be

acquired from airborne/terrestrial photogrammetry or laser scanning. In particular Light-Detection and Ranging (LiDAR) is being employed in an increasingly large number of applications providing very accurate surface representations because of its capability to penetrate vegetation and to acquire very dense and precise point clouds (Heritage and Large, 2009; Jaboyedoff et al., 2010). However, the costs of the equipment and the logistics of LiDAR surveys are currently still rather high and acquisitions at high temporal resolution are, therefore, not always feasible. Conventional photogrammetric techniques with metric and non-metric cameras are a frequently employed alternative for a wide range of applications (Fryer et al., 2007) but comprise high demands on the image acquisition geometry, ground control, processing software and the experience of the operator (Henry et al., 2002; Fryer et al., 2007).

Great advances of the photogrammetry and computer-vision communities in pose-estimation and bundle-adjustment (Triggs et al., 2000; Hartley and Zisserman, 2004), camera self-calibration (Fraser, 1997; Pollefeys et al., 1999) as well as feature-based and area-based image matching (Lowe, 2004; Pierrot-Deseilligny and Paparoditis, 2006; Hirschmuller, 2008; Furukawa and Ponce, 2010) have recently converged in a new class of photogrammetric algorithms that enable more flexible 3D surface reconstruction from unordered non-metric image collections. These tools are summarized under the terms 'Structure-from-Motion' (SfM i.e. the process of estimating camera parameters and sparse point-clouds; Ullman 1979) and Multi-View Stereo (Seitz et al., 2006), (MVS, i.e. the process of deriving dense surface models once the correspondence among multiple cameras has been established). Many proposed approaches for SfM and MVS are implemented in commercial softwares (e.g., AgiSoft PhotoScan, Pix4D, PhotoModeler Scanner, and Trimble Inpho), web-based services (e.g., Microsoft Photosynth, Autodesk 123D, Arc3D, and Cubify Capture) and in open-source or freely available software packages (Snavely et al., 2008; Furukawa and Ponce, 2010; Deseilligny and Clery, 2011; Rothermel et al., 2012; Wu, 2013).

The geoscience community has already taken great interest in these new tools (James and Robson, 2012; Westoby et al., 2012; Fonstad et al., 2013) and recent applications in geomorphology include

landslide investigation (Niethammer et al., 2011; Lucieer et al., 2014), costal cliff monitoring (James and Robson, 2012), lava flow and volcanic dome analyses (James and Varley, 2012; Bretar et al., 2013), glacial and periglacial processes research (Kääb et al., 2013; Whitehead et al., 2013), gully erosion surveys (Gómez-Gutiérrez et al., 2014), soil microtopography (Ouédraogo et al., 2014) and braided river systems (Javernick et al., 2014).

These studies have shown that among many factors that condition the accuracy of SfM-MVS (e.g. camera, lens, and acquisition geometry, quality of the ground control, illumination, and processing software), the distance to the object is probably the most influential. Imaging distances between < 2 m (Bretar et al., 2013) and > 2000 m (James and Robson, 2012) have been explored resulting in accuracies that are generally between 0.04 and 1.68 m, respectively. James and Robson (2012) suggested a relative precision of 1:1000 corresponding to an *RMSE* value of 1 m at an imaging distance of 1000 m. However, limited attention has been paid to comparisons of different processing pipelines (Ouédraogo et al., 2014). While several benchmark studies have evaluated MVS algorithms on toy models (Seitz et al., 2006) and architectural outdoor scenes (Strecha et al., 2008; Remondino et al., 2012), there is currently no corresponding information for natural terrain available. Natural scenes yield fundamentally different image characteristics (Torralba and Oliva, 2003) and are typically more challenging in terms of surface features, illumination and constraints on the viewing geometry. For interested users, it is consequently difficult to select the most accurate solution among the variety of available tools. This also applies, to some extent, for the choice of the algorithm parameters whose values are typically not reported in the literature.

In susceptible lithologies and landscapes, landslides can dominate the sediment transfer (Hovius et al., 2000; Mackey and Roering, 2011); however, it is in general still challenging to obtain measurements of the kinematics and sediment budgets with high spatio-temporal coverage. Travelletti et al. (2012) and Gance et al. (2014) have recently demonstrated that terrestrial time-lapse photography is a valuable tool for the monitoring of slow-moving landslides; Niethammer et al. (2011) and Lucieer et al. (2014) provided examples for the use of UAV-based SfM-MVS to monitor landslide deformation

from two acquisitions. Since terrestrial multi-view photogrammetry does not depend on aerial platforms or fixed permanent terrestrial installation, it could provide a very flexible tool for the monitoring of landslides and other geomorphological processes at high temporal and spatial resolution.

Therefore, the target of this work is to evaluate quantitatively the accuracy of dense point clouds created from several SfM-MVS pipelines (Deseilligny and Clery, 2011; Wu et al., 2011; Deseilligny et al., 2013; Wu, 2013) for 3D landslide surface monitoring including the measurement of surface deformation as well as the quantification erosion rates. The paper is organized as follows: First, the study site (Super-Sauze landslide) is introduced together with the acquisition protocols of the terrestrial photographic surveys, and the ground-control datasets obtained from LiDAR and differential GPS (dGPS) surveys are explained in detail. Second, details of three SfM-MVS algorithms and pipelines are presented. Third, the accuracy of the photogrammetric models is assessed through comparison with LiDAR point clouds. Fourth, change detection methods are applied to quantify the surface changes and the dynamics of the landslide over a period of two years. Finally, current limitations, potentials and possible pitfalls of the processing pipelines and image acquisition protocols are discussed.

2. Study site and data acquisition

The Super-Sauze landslide (Fig. 1) is a clay-rich slow-moving slope movement located in the Southern French Alps. The landslide initially developed in the 1960s through retrogressive failures of the main scarp; at present, its dynamics are controlled by the local hydrology-meteorological conditions and the accumulation of new material from successive failures at the main scarp. During the last decade, several in-situ and remote sensing studies have contributed to a better understanding of the movement pattern (e.g. Malet et al., 2002; Niethammer et al., 2011; Travelletti et al., 2012;

Stumpf et al., 2013). For further information on the regional climatic and geological context the interested reader is referred to Flageollet et al. (1999). Multi-technique displacement observations since 1996 suggest an average displacement rates of 0.01–0.03 m d^{-1} (Malet et al., 2002) but regularly, daily cumulative displacements larger than 5 m are observed (Travelletti et al., 2012). Such relatively high displacement rates pose challenges for displacement measurements since they often lead to signal decorrelation in the multi-temporal analysis of radar and optical images, and hinder the long-term maintenance of in-situ measurement devices.

The site is characterized by a rugged topography comprising vertical and overhanging cliffs, thalwegs and depressions of various sizes, and quasi-horizontal surfaces. The eastward-adjacent slopes are largely forested, whereas the westward-adjacent slopes consist of badlands, sub-parallel ridges bordering the landslide. Constraints on possible camera view points, low incidence angles and topographic or vegetation occlusion make such type of terrain very challenging for terrestrial photogrammetric measurements.

Acquisitions of terrestrial photographs in an MVS setup have been carried out since October 2011 at regular intervals (Table 1). Field campaigns are typically limited to the time between early May and late October since snow cover prohibits photogrammetric and most other measurements during the rest of the year. A Nikon D700 camera has been used, the focus has been set to infinity, and care has been taken to obtain a good trade-off between sufficiently short exposure time and large depth of field (narrow aperture) for all acquisitions.

Two target zones were monitored by photogrammetry. A first acquisition protocol was setup to reconstruct the evolution of the main scarp (Fig. 1) at five dates for the period October 2011 till July 2013. The images were recorded in a surface-parallel linear array of panoramic shots with distances to the targeted surface between 20 and 200 m. During the first survey images were recorded only at a reduced resolution (2128×1416) and in JPEG format, whereas for all subsequent surveys full resolution (4256×2832) images were stored in native Nikon (NEF) file-format to avoid information

loss. A 60 mm lens was used at all dates except in July 2012 when a 35 mm lens was used to also investigate the influence of the focal length on the reconstruction.

A second acquisition protocol was setup to obtain a full-scene model for the entire landslide on 10-Oct-2012 and 19-Jul-2013. Images were captured in a half circular array along the limits of the landslide (Fig. 1) using a 35 mm lens. Distances to the targeted surface varied between approximately 50 and 1000 m. The latter constitutes a rather great distance for the application of terrestrial photogrammetry and according to James and Robson (2012) an *RMSE* value of 1 m should be expected.

The point clouds used as a reference dataset were acquired with a terrestrial (Optech ILRIS-3D) and an airborne (Riegl LMS-Q560) laser scanner. To provide full coverage of the main scarp, multiple terrestrial scans were acquired from different view angles aligned subsequently using the Iterative Closest Point (ICP) algorithm implemented in PolyWorks (Innovmetric, 2010). The scans were performed at an average distances between 3 and 800 m resulting in a ground-point density of ca. 100 points m^{-2}. The scan accuracy (standard deviation) of the terrestrial LiDAR scans (TLS) varies between ~0.01 m at 100 m and ~0.02 m at 2000 m (Abellán et al., 2013), whereas the alignment error amounts to an *RMSE* value of 0.02–0.03 m (Travelletti, 2011). The airborne LiDAR scan (ALS) was acquired on 29-Aug-2012 with an average flight height of 800 m above the surface resulting in an average ground-point density of approximately 90 points m^{-2}. The accuracy of the airborne point-cloud is influenced by scanning, georeferencing and reprojection errors and typically ranges between 0.20–0.30 m (Travelletti, 2011). The resulting point cloud and associated orthophotographs were used to visually identify 34 GCPs on salient natural objects (sharp edges of boulders) located on stable slopes outside the landslide. Despite the time lag of 42 days between the ALS and the MVS image acquisitions in October 2012, the selected targets where considered as stable since in recent years ground deformation at the site has been confined to the active areas delineated in Fig. 1. In addition, the coordinates of 39 artificial ground targets (of size 0.5×0.5 m) were measured during the image acquisitions in July 2013 using dGPS. The dGPS survey was carried out with a Trimble R7 geodetic

receiver in post-processes kinematic mode using an acquisition frequency of 1 Hz. The survey time on each target was 10 minutes, corresponding to the collection of 600 epochs per target. The post-processing was performed with the GAMIT software using a network of three permanent base stations, with baseline lengths between 600 and 5000 m. The maximum elevation difference among the base receivers and the mobile receivers is 350 m. The 3D measurement error of the dGPS survey is of 2.5 cm in the three components.

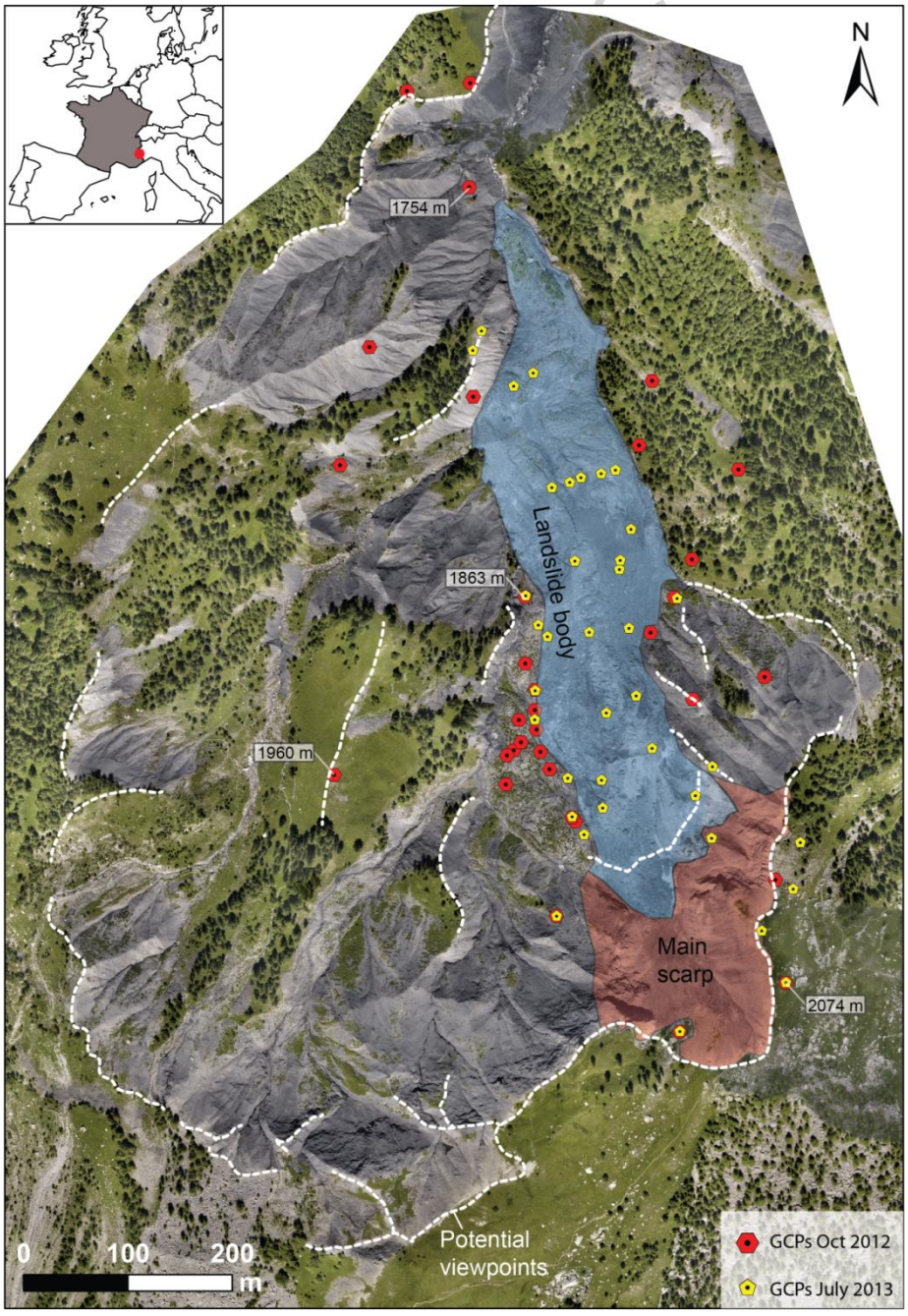

Fig. 1. Location and general structure of the Super-Sauze landslide. The possible view points for the MVS image acquisition and the GCPs used for georeferencing the dataset at two acquisition dates are indicated.

Table 1. Overview of the collected data during the MVS image acquisition, LiDAR and dGPS surveys.

Date	**Images main scarp**	**Terrestrial LiDAR**	**Images landslide body**	**Airborne LiDAR**	**dGPS**
	Number of images Focal length Size	Scanner/ Distance Point density $RMSE_{xyz}$	Number of images Focal length Size	Scanner / Distance Point density $RMSE_{xyz}$	Receiver / Baseline Measurement time $RMSE_{xyz}$
20-Oct-2011	88 60 mm 2128×1416	ILRIS-3D, 3–800 m > 100 pts m^{-2} 0.02–0.03			
5-Jul-2012	106 35 mm 4256×2832	ILRIS-3D, 3-800 m > 100 0.02–0.03 m			
29-Aug-2012				LMS-Q560 / ~800 m ~ 90 pts m^{-2} 0.20–0.30 m	
9-Oct-2012	168 60 mm 4256×2832	ILRIS-3D, 3-800 m > 100 pts m^{-2} 0.02–0.03 m			
10-Oct-2012			401 35 mm 4256×2832		
14-May-2013	130 60 mm 4256×2832				
18-Jul-2013	265 60 mm 4256×2832				Trimble R7 / 600–5000 m 10 min 0.03 m
19-Jul-2013			401 35 mm 4256×2832		Trimble R7 / 600–5000 m 10 min 0.03 m

3. Processing methods

3.1 Photogrammetric reconstruction

All surface reconstruction pipelines are based on open-source libraries and follow a common SfM-MVS sequence including the extraction of homologous image points, the estimation of camera parameters and the bundle adjustment (Fig. 2a,b); the dense reconstruction is performed in a subsequent step (Fig. 2c).

VisualSfM (VSfM) is a freely-available software implementing algorithms for point matching using the Scale Invariant Feature Transform (SIFT, Lowe, 2004) on Graphical Processing Units (GPUs) (Wu, 2007), pose-estimation and multi-core bundle adjustment (Wu et al., 2011; Wu, 2013) for which the source code is also partially available. PMVS2 is a patched-based multi-view stereo algorithm (Furukawa and Ponce, 2010) targeting dense reconstruction after camera correspondence has already been established. The algorithm can be scaled to large reconstruction problems using a related cluster multi-view stereo (CMVS) algorithm (Furukawa et al., 2010).

MicMac is an open-source software project for multi-view photogrammetry (Deseilligny et al., 2013). The project comprises tools for tie-point extraction (Tapioca), pose-estimation, camera-calibration, bundle-adjustment (Apero, Deseilligny and Clery, 2011), dense-matching (MicMac, same as the entire library) and georeferencing; this library also offers various tools dedicated to point cloud extraction, creation of masks, and orthorectification.

Three different pipelines combining (a) VSfM with CMVS (VSfM+CMVS), (b) Apero with CMVS (Apero+CMVS), and (c) Apero with MicMac (Apero+MicMac) were compared against aerial and terrestrial LiDAR scans in terms of completeness and accuracy of the reconstruction. As a general strategy for the use of Apero, 10 to 15 images were selected for lens self-calibration; the bundle adjustment was repeated several times adding images successively, while keeping the lens model fixed and using the estimated poses from the previous run for initialization. It was targeted to integrate all collected images; however, views with high residuals, blur or unfavorable illumination conditions

were removed for the final bundle adjustment aiming at a reduction of the residuals below 0.5 pixel. All surface reconstructions were performed on a workstation with 8 cores, 36GB RAM and an NVIDIA Quadro 600 GPU in a Linux 64 bits environment. An overview of the processing steps is provided in Fig. 2; all further technical details on the different reconstruction algorithms are provided in the Supplementary material for online publication A–C.

The dense point clouds from the three pipelines were analyzed in Meshlab (Cignoni et al., 2008). Obvious outliers (point patches far from the average surface, unnatural correlation artifacts) were manually removed (Fig. 2d). Both CMVS and MicMac typically yield overlapping point clouds originating from multiple view clusters and base images, respectively. Redundant points in these overlapping areas were removed and preference was given to the point clouds with higher density.

3.2 Georeferencing

Two georeferencing techniques were used according to the availability of GCPs at the time of the MVS image acquisition. For the dataset of July 2013, precise GPS measurements on photogrammetric targets were recorded at the landslide body and main scarp; for the dataset of October 2012, GCPs over stable terrain were obtained from temporally close ALS (Section 2). For these dates the georeferencing was performed with the MicMac library, which comprises a graphical interface to mark the position of the GCPs directly in the photographs. The marked GCPs and the automatically extracted tie points were subsequently introduced in Apero in order to resolve the exterior camera parameters in the terrain coordinate system. The uncertainty of the ground and image measurements was provided by the users and constitutes weights for the least-square optimization. Table 2 summarizes the number of used GCPs and their respective uncertainties, which were set according to the errors of the respective reference measurements. This method is further referred to as *GCP-based georeferencing* (Fig. 2b).

Table 2. Summary of the ground control used for GCP-based referencing

	Full Scene 9-Oct-2012	**Full Scene 19-Jul-2013**	**Main scarp 18-Jul-2013**
GCP source	Orthophotograph + ALS (salient objects on stable areas)	dGPS measured targets	dGPS measured targets
Number	34	39	11
Ground uncertainty	0.25 m	0.05 m	0.05 m
Image uncertainty	1 pixel	0.5 pixel	0.5 pixel

For four models of the main scarp (20-Oct-2011, 5-Jul-2012, 9-Oct-2012, and 14-May-2013), no GCPs were available and the dense reconstruction was performed using an image coordinate system. The point clouds were subsequently referenced to a terrain coordinate system through semi-automatic matching relative to existing georeferenced point clouds. For the dates 20-Oct-2011, 5-Jul-2012 and 9-Oct-2012, the terrestrial laser scans recorded at the same date were used. The model generated for 14-May-2013 was georeferenced with respect to the photogrammetric point cloud derived for 18-Jul-2013 considering only stable terrains in the alignment. A coarse initial alignment (rotation, translation, and scaling) was achieved based on four homologous points that were selected manually, and the ICP algorithm implemented in Polyworks was used subsequently to refine the alignment (rotation and translation). This approach is further referred to as *relative georeferencing* (Fig. 1e). It is noteworthy that the area of interest at the main scarp is completely free of vegetation which is an important prerequisite for an accurate ICP-based registration.

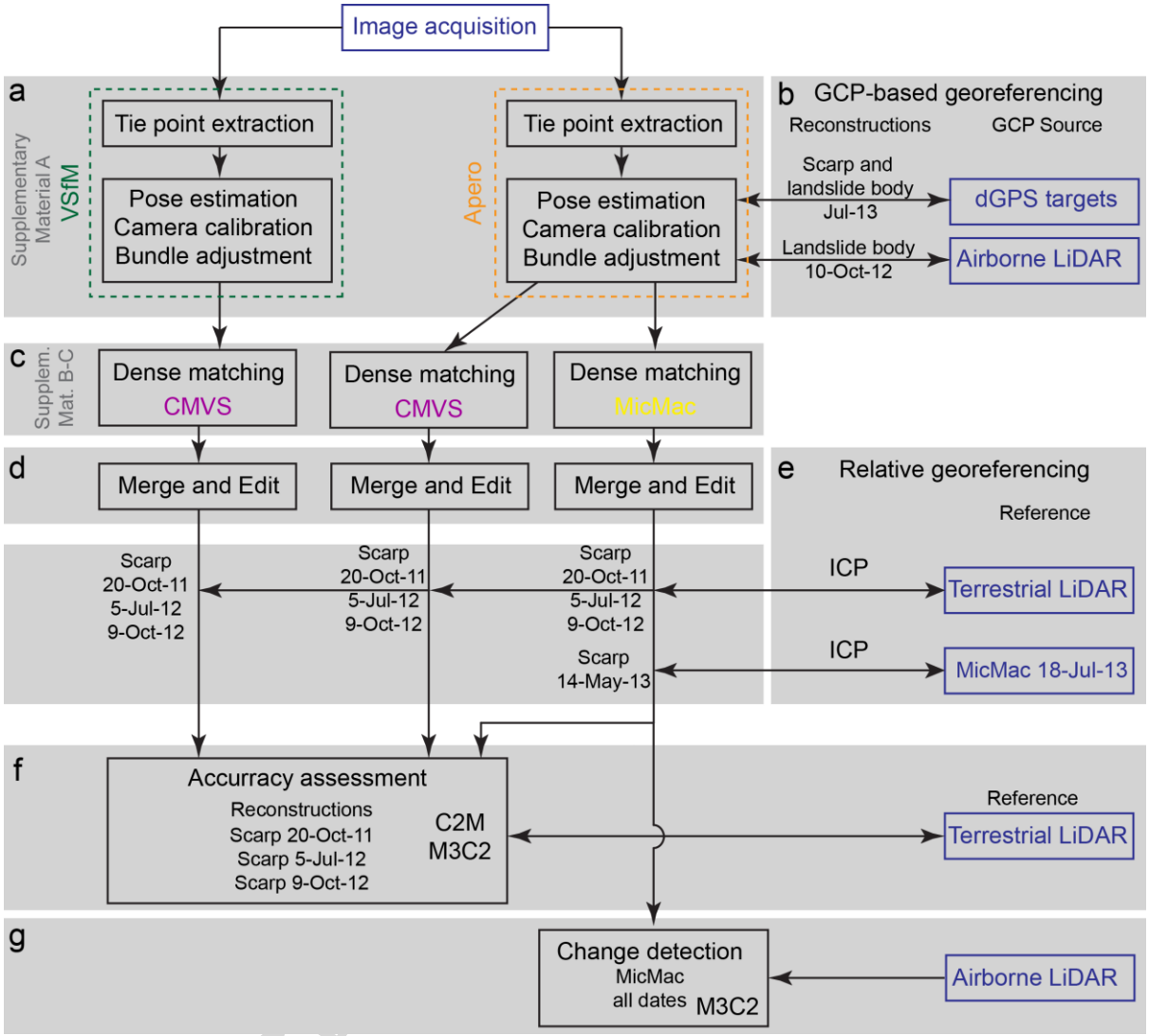

Fig. 2. Generalized workflow for the reconstruction pipelines, accuracy assessment and change detection. The analysis comprises (a) tie point extraction and the estimation of interior and exterior camera parameters, (b) GCP-based georeferencing of dates for which Ground Control Points (GCPs) are available, (c) dense point cloud extraction, (d) manual editing, (e) relative georeferencing of dates on which no ground control is available, (f) accuracy assessment against TLS, and (g) change detection for the full time series. See text and Supplementary Material for details on the employed algorithms.

3.3 Accuracy assessment

To quantify the accuracy of photogrammetric reconstruction it is indispensable to compare the resulting surfaces against reference measurements whose measurement error is known and as low as possible. While long GPS observation sessions (typically > 3 hours) can yield millimetric accuracy (Malet et al., 2002), short sessions during photogrammetric campaigns typically comprise errors in the range of several centimeters. Especially in complex landscapes, it should further be considered that Ground Control Points (GCPs) cannot be measured on very steep slopes and rugged surfaces introducing a potential bias. Terrestrial and airborne LiDAR scans provide spatially distributed point clouds at accuracies between 0.01 and 0.15 m, respectively (Jaboyedoff et al., 2010; Abellán et al., 2013) and have been used to assess the error of SfM-MVS techniques in several studies. In many cases, the obtained points clouds are interpolated to continuous surface before comparison (Dandois and Ellis, 2010; Niethammer et al., 2011; James and Robson, 2012; Westoby et al., 2012; Fonstad et al., 2013; Ouédraogo et al., 2014) which is not ideal since interpolation artifacts may bias the accuracy estimates. Another commonly used approaches for point-cloud comparison is to interpolate a surface from one of the two point clouds and compute the distance along the surface normal (cloud-to-mesh, C2M; Girardeau-Montaut et al., 2005). This approach generally provides very accurate distance measurements (Lague et al., 2013) but poses problems in areas where the two point clouds do not overlap. The distances among the closest points in the meshes are typically overestimated where the reference point cloud contains no or very few points (Barnhart and Crosby, 2013; Lague et al., 2013). To obtain accurate measurements, it is hence necessary to remove all non-overlapping areas during time-consuming manual editing.

Lague et al. (2013) proposed a technique (M3C2, Multiscale Model to Model Cloud Comparison) that does not require an explicit surface interpolation but estimates the surface normals and distances directly from the point clouds. In a first step the surface normals at each point are computed considering all points in a neighborhood of the size $D/2$ (D is the scale factor). The normals can be

computed from one reference cloud (typically the earlier date) or by averaging the normals of the two point clouds. Subsequently, the distances are calculated at each point as the mean distance between all points in a neighborhood of the size $d/2$ (d is the projection scale). An additional parameter p_{max} defines the length of the projection cylinder and thereby the maximum distance between points considered in the computation. The scale D should be chosen sufficiently large to guarantee that the distance measurement is independent of the surface roughness, and a range of d of 0.3–2 m is recommended (Barnhart and Crosby, 2013; Lague et al., 2013).

To assess the accuracy of the point clouds obtained with the three SfM-MVS pipelines, the datasets were compared against the TLS taken at the same date and with ALS over stable terrain. For the accuracy assessment, we focused on the first three acquisitions at the main scarp and tested both comparison methods (C2M and M3C2). In order to obtain accurate and comparable results, non-overlapping parts of the point clouds were removed manually beforehand and the C2M algorithm implemented in CloudCompare (EDF-R&D, TelecomParisTech, 2013) was used. Two techniques were considered to interpolate the reference mesh for C2M from the LiDAR point clouds: a simple Delaunay Triangulation with a least-square local plane fit, and a screened Poisson surface reconstruction (Kazhdan and Hoppe, 2013). Since the Poisson reconstruction resulted in an overly smooth surface and consequently higher distances between the LiDAR mesh and the photogrammetric point clouds only the results of the Delaunay Triangulation were reported. The parameters for the M3C2 algorithm were adapted according to the surface roughness and the maximum expected changes. Since the surfaces are relatively similar, rather small values for D and p_{max} were sufficient. Previous studies on the use of photogrammetric techniques for geomorphological applications (Section 1) indicate that LiDAR still provides more accurate surface representations than MVS and the LiDAR point clouds were therefore used to compute the orientation of the surface normals. Table 3 comprises the selected parameter settings for the accuracy assessment at the main scarp.

3.4 Change detection

M3C2 provided the more reliable accuracy estimates (see Section 4.2) and was therefore used for the detection of changes over time. Since the general shape and roughness of the surface may vary considerably between the acquisition dates, larger scale parameters were selected to promote a greater robustness of the distance calculation. For the same reason, the normals were estimated as the average from both point-clouds. An interesting feature of the M3C2 algorithm is the possibility to estimate a 95%-confidence interval for significant changes between two point clouds. The calculation of the confidence interval is based on the local surface roughness and the registration error which can be set to account for both referencing and measurement errors (see Lague et al., 2013 for further details). Table 3 details the selected parameter settings for the accuracy assessment at the main scarp.

Table 3. Parameter settings for the M3C2 algorithm for the accuracy assessment and the change detection.

M3C2 parameter	**Accuracy assessment: main scarp**	**Change detection: target main scarp**	**Change detection target: landslide body**
D	5 m	10 m	15 m
d	0.5 m	1.0 m	1.5 m
p_{max}	5 m	7 m	7 m
Normal computation	LiDAR	Average normal from both point clouds	Average normal from both point clouds
Registration error for change detection	-	0.1 m	0.2 m

Volume budgets can be derived from vertical distance measurements through interpolation and subtraction of two horizontal grids (e.g. Wheaton et al., 2010). However, since steep cliffs and overhanging rock walls are not well represented when projected on a horizontal grid, a plane fitting

algorithm was employed to adapt the orientation of the raster grid locally to the surface (for further details see Supplementary Material D). Volumes and their respective uncertainties were derived directly from the M3C2 distances and the corresponding 95% confidence intervals.

Existing methods to obtain 3D displacement from point clouds have been developed mainly for the processing of LiDAR point clouds. They are applicable if the surface deformation is relatively small and homologous features are well preserved among multiple time steps (Teza et al., 2007; Monserrat and Crosetto, 2008; Aryal et al., 2012) or if the multi-date point clouds have been recorded from the same viewing position (Travelletti et al., 2014). These conditions are not satisfied considering the large deformation observed in this study and the variable viewing geometry of the MVS setup. As a consequence 3D displacement vectors were derived through a combination of initial manual piecewise alignment of salient objects and a subsequent fine registration using the ICP algorithm.

4. Results and discussion

To evaluate the accuracy of the three pipelines, the results were compared to the corresponding terrestrial and airborne LiDAR scans; the Mean-Absolute Error (MAE), the Root-Mean-Squared Error (RMSE) and the Mean Distance (MD) between the clouds are reported. While the MD does not reflect the accuracy of the 3D model, it provides a useful indicator for a potential bias after geroreferencing and co-registration. The subsequent sections provide a general overview of the results of the reconstruction and georeferencing (Section 4.1), the outcomes of the accuracy assessment comparing the three different pipelines at the main scarp (Section 4.2), an analysis of the detected changes over time (Section 4.3) and a detailed discussion of the potential and limitations of SfM-MVS for landslide monitoring (Section 4.4).

4.1 Photogrammetric reconstruction and georeferencing

Quality indicators for all reconstructed models are provided in Table 4. Comparing the number of points obtained with the three pipelines Table 4 indicates that MicMac provides significantly denser point clouds and greater coverage (see Section 4.3.1). Beside these indicators it is noteworthy that for the full scene acquisition of 9-Oct-2012, a block of 69 images remained unconnected and could not be used for further modeling. VSfM allowed us to use most images for the modeling of the main scarp (20-Oct-2011, 5-Jul-2012, and 9-Oct-2012) but did not succeed to integrate sufficient images for the modeling of the entire landslide.

Table 4. Quality indicators for the photogrammetric reconstructions and dense point clouds and residuals of the GCP-based georeferencing with Apero.

	Main scarp 20-Oct-2011	**Main scarp 5-Jul-2012**	**Main scarp 9-Oct-2012**	**Full scene 9-Oct-2012**	**Main scarp 14-May-2013**	**Main scarp 18-Jul-2013**	**Full scene 19-Jul-2013**
Reconstructed views (total) with Apero	84 (88)	106 (106)	142 (168)	332 (401)	130 (130)	244 (265)	401 (401)
Global residuals (pixel)	0.458	0.325	0.497	0.460	0.474	0.496	0.433
Reconstructed views (total) with VSfM	82 (88)	106 (106)	164 (168)	209 (401)	-	-	-
Number of points with							
VSfM+CMVS	1,646,455	12,679,042	12,645,586	-	-	-	-
Apero+CMVS	1,693,774	15,563,370	15,843,093	-	-	-	-
Apero+MicMac	14,233,097	27,613,581	23,628,364	44,395,642	49,971,598	67,042,957	48,378,876
Residuals of GCP-based referencing (GCP source)	-	-	-	0.32 ± 0.20 m (ALS)	-	0.10 ± 0.05 m (dGPS)	0.05 ± 0.04 m (dGPS)

The results of the GCP-based georeferencing with Apero are reported in Table 4 and it can be seen that the residuals correspond strongly with the uncertainty of the respective GCPs (Table 1). Using the GCPS derived from the ALS with an *RMSE* value of 0.2–0.3 m, the residuals amount to 0.32 m, whereas the dGPS based referencing yields residuals of only 0.05 to 0.10 m. Table 5 indicates that for the models of the main scarp, the MD is at most 1.6 cm and generally below 0.07 cm which is in all cases only a minor fraction of *RMSE*. All other models are referenced using relative georeferencing as described above.

In general, GCP-based georeferencing during bundle adjustment is a more convenient strategy than relative georeferencing, since it is more straightforward and accurate to locate GCPs on the photographs than within the point clouds. Furthermore, additional processing within other software can be avoided. However, a visual inspection of the stable areas in the photogrammetric models of the entire landslide (9-Oct-2012 and 19-Jul-2013) and the ALS point cloud revealed a small systematic residual misalignment. This could be attributed to errors in the georeferencing of the ALS data which generally exceeds the scan error and, therefore, dominates the absolute error in the point location (Ussyshkin and Smith, 2006). To correct this systematic offset the ICP algorithm was employed to estimate a global translation aligning the ALS point cloud to the photogrammetric reconstruction of 19-Jul-2013. For this operation only points on stable terrain and without vegetation were taken into account. After this alignment, the MD between the photogrammetric models and the ALS point cloud reduced to 1.1–3.2 cm on the stable areas (Table 5).

4.2 Accuracy of the point clouds generated from the SfM-MVS pipelines

A comparison of the three tested SfM-MVS pipelines is provided considering the first three reconstructions of the main scarp (20-Oct-2011, 5-Jul-2012, and 9-Oct-2012) which were aligned to the respective terrestrial LiDAR point clouds using relative georeferencing as described in Section 3.2. The two tested methods for the distance computation (C2M and M3C2) provide very similar

results, though M3C2 results in slightly lower error estimates (the maximum *RMSE* difference between both methods is 1.6 cm). Manual masking of the non-overlapping areas is a pre-requisite for the application of C2M, and larger error estimates are likely if small non-overlapping areas have not been recognized correctly. Consequently, the M3C2 is considered as the more reliable estimator and used for change detection throughout the rest of the study. It is also used to assess the registration error between the photogrammetric models of the entire landslide and the ALS over stable slopes which are free of vegetation.

For the models of the scarp the *RMSE* values measured with M3C2 (Table 5) are between 2.7 and 7.5 cm. Apero+MicMac provides the most accurate point clouds (*RMSE* of 2.7–5.6 cm) while VSfM+CMVS yield slightly higher errors (*RMSE* of 5.7–7.5 cm). The best match between the Apero+MicMac reconstruction and the TLS was observed for acquisition of 5-Jul-2012 with an *RMSE* value of only 2.7 cm (Fig. 3c). Considering that the uncertainty of the TLS is already within the range of 2–3 cm, it is, at least in this case, not possible to state with certainty if the LiDAR or the photogrammetric point cloud provide a more accurate representation of the surface. The Apero+CMVS pipeline provided accuracies similar to VSfM+CMVS except for 5-Jul-2012 where it improves *RMSE* by 1.3 cm. This is probably related to the fact that a 35 mm lens with greater distortion was used for this acquisition, and the more complex lens model used in Apero compensates the distortion better than the simple lens model used in VSfM.

All the three pipelines provided the most accurate results for the acquisition with the 35 mm lens (Fig. 3). This is somewhat surprising since the greater lens distortion and the increased ground sampling distance could be expected to lower accuracies in comparison to acquisitions realized with the 60 mm lens. At the same time, acquisitions with a 35 mm lens provided generally greater overlap among the different views which lead to better redundancy of the tie-point network. This in turn promotes lower residuals of the pose estimations (see residuals in Table 4) which apparently overcompensates the influence of the increased lens distortion and ground sampling distance. A closer inspection of Fig. 3 reveals that the errors globally follow a narrow normal distribution. However, in

particular for the VSfM+CMVS model (Fig. 3a) negative and positive deviations are rather spatially clustered. Such local biases of the reconstruction are not taken into account by the change detection technique which assumes a spatially homogenous distribution of the errors, and consequently, can either lead to false positives or to a masking of real changes.

While all three pipelines provided comparable results, Apero+MicMac yielded higher accuracies, better coverage as well as higher point density, and is the only technique that allowed a satisfactory reconstruction of the entire landslide. It is important to note that VSfM and CMVS were developed for large scale reconstructions from unordered image collections and require less manual intervention and computing time. However, the final accuracy of the models is considered as a more important factor in the context of this study and, therefore, Apero+MicMac was used for the processing of the remaining models.

Considering the results of the accuracy assessment at the main scarp, models for the entire landslide were generated using the Apero+MicMac processing chain. To assess their accuracy, model sections on stable slopes and free of vegetation were compared to the ALS of 29-Aug-2012 using the M3C2 algorithm. The *RMSE* value of those areas is between 0.20 and 0.23 m (Table 5).

Table 5. Accuracy assessment of the different processing pipelines for the models at the main scarp at three dates using M3C2 and C2M (values in brackets) for the distance estimation (best results in bold). For the entire landslide, results were only obtained with Apero+MicMac.

Model	Reference	Error Measure	VSfM+CMVS	Apero+CMVS	Apero+MicMac
Main scarp 20-Oct-2011	TLS (same date)	MAE [m]	0.044 (0.046)	0.038 (0.041)	**0.031 (**0.038)
		RMSE [m]	0.075 (0.086)	0.075 (0.085)	**0.056 (**0.060)
		MD [m]	0.002 (0.002)	0.016 (0.013)	0.006 (0.006)
Main scarp 5-Jul-2012	TLS (same date)	MAE [m]	0.029 (0.029)	0.022 (0.024)	**0.016 (**0.019)
		RMSE [m]	0.057 (0.073)	0.044 (0.050)	**0.027 (**0.027)

		MD [m]	0.000 (0.001)	0.007 (0.004)	0.000 (0.000)
Main scarp 9-Oct-2012	TLS (same date)	MAE [m]	0.038 (0.040)	0.033 (0.034)	**0.033 (**0.039)
		RMSE [m]	0.066 (0.063)	0.067 (0.060)	**0.050 (**0.050)
		MD [m]	−0.002 (−0.003)	0.006 (0.002)	−0.005 (−0.004)
Entire landslide 10-Oct-2012	ALS (29-Aug-2012) stable areas without vegetation	MAE [m]	-	-	0.143
		RMSE [m]	-	-	0.204
		MD [m]	-	-	-0.032
Entire landslide 19-Jul-2013	ALS (29-Aug-2012) stable areas without vegetation	MAE [m]	-	-	0.134
		RMSE	-	-	0.232
		MD	-	-	0.011

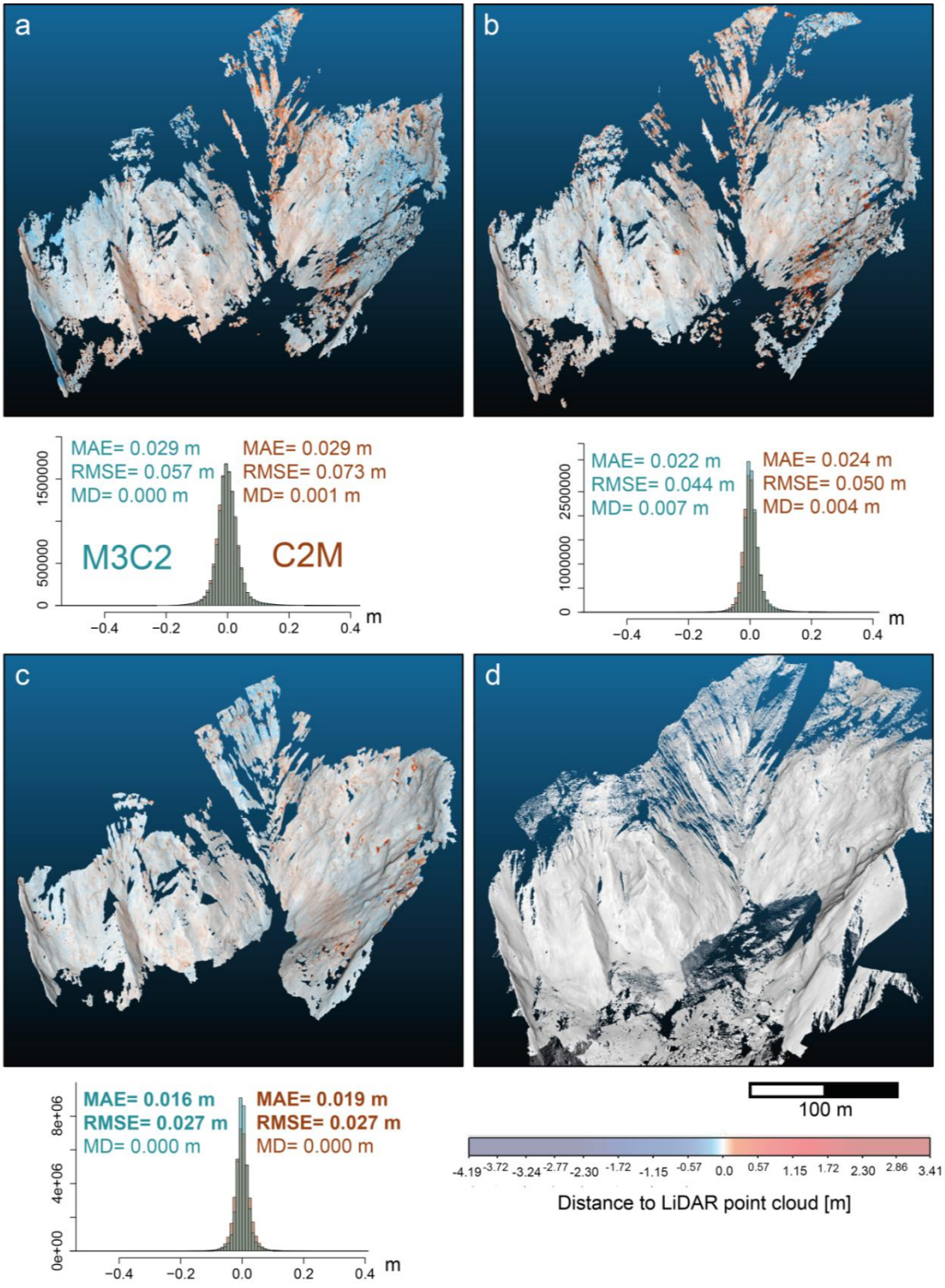

Fig. 3. Comparison of the photogrammetric reconstructions using (a) VSfM+CMVS, (b) Apero+CMVS, and (c) Apero+MicMac against (d) TLS of 5-Jul-2012. MAE, RMSE and MD from

two tested point-cloud comparison methods are reported. Since the images provide a perspective view, the scale bar only provides average values.

4.3 Temporal evolution of the Super-Sauze landslide

The results of the change detection (M3C2) are analyzed in order to infer the deformation pattern of the landslide during the monitoring period. The deformation pattern comprises a combination of a creeping/sliding behavior of the mass and as well as superficial processes such as small slumps or rockfall events. Based on the point cloud analysis, first order estimates of the released and transferred sediment volumes are provided. The uncertainties of the reported volumes are derived from the 95% confidence interval on the measured M3C2 distances. The possibility to obtain 3D displacement vectors is illustrated exemplarily for the most active region of the landslide.

4.3.1 Retrogression of the main scarp: quantification and interpretation

Fig. 4 provides a perspective view of the main scarp indicating areas of major changes. Among the detected changes it is possible to distinguish three main components: volume loss at the rock wall, volume gain at the scree slopes and volume loss at the scree slopes. These components are distinguished to provide a differentiate interpretation of the dynamics and a quantification of the detected changes. Over the monitored period, significant changes were observed for all time intervals (Fig. 5) and the maximum detected differences amounted to between –5.7 m (ablation) and 7.1 m (sediment accumulation). The minimum change detected at 95% confidence is 0.2 m since the co-registration error is 0.1 m (Table 3).

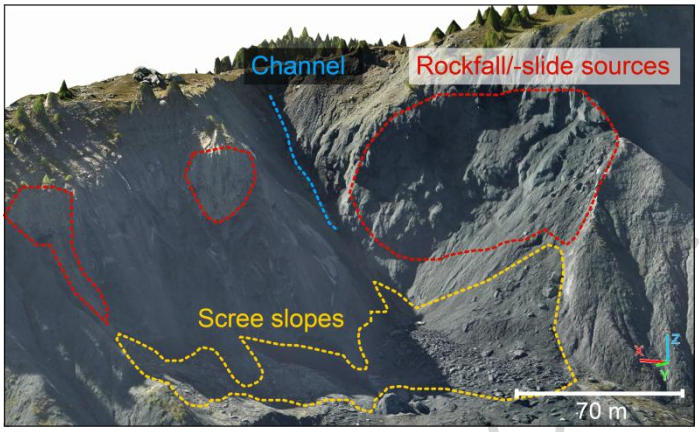

Fig. 4. Synthetic view (ALS and orthophotograph 29-Aug-2012) of the main scarp indicating areas with major detected changes. The scale bar is an average value for this perspective view.

From Table 6, it can be seen that the coverage obtained from the first two photogrammetric surveys was not fully satisfactory but has been successively increased from the experience of the previous surveys. The coverage has been computed as the percentage of terrestrial LiDAR point clouds that could be projected on the photogrammetric point clouds with the M3C2 algorithm.

Hence, due to limited mutual coverage of the photogrammetric models, the amount of detected changes and the estimated volume budgets provide only a lower bound on the actual changes. This is particularly true for the first two periods (20-Oct-2011 to 5-Jul-2012 and 5-Jul-2012 to 9-Oct-2012), whereas due to the enhanced coverage after 9-Oct-2012, the computed changes and volume budgets can be considered reliable within the provided confidence intervals.

Table 6. Coverage of the photogrammetric models of the main scarp relative to the TLSs.

Date	20-Oct-2011	5-Jul-2012	9-Oct-2012	14-May-2013	18-Jul-2013
Coverage (% of projected LiDAR points)	43%	63%	76 %	73%	81%

The first period (8.5 months, autumn to early summer) was dominated by a loss of volume at the rockwall resulting from rockslides and rockfalls and a removal of loose material from the scree slopes through water runoff. The source of a medium-size rockslide with a released volume of 1.01×10^3 ±110 m^3 (compared to 960 ± 120 m^3 from the LiDAR-based survey) is detected at the eastern part of the rockwall (Fig. 5a). Since the western part of the rockwall is only partially covered by the photogrammetric survey of 20-Nov-2011, a large size rockslide that occurred was not detected. An analysis of the corresponding terrestrial LiDAR scans suggests that the rockslide released 15.44×10^3 ± 710 m^3 of material, which strongly dominates the volume budget and explains the strong deviation between the LiDAR- and MVS-based volume budgets for this period (Fig. 5a).

During the following period (~3 months, summer to autumn), only minor (< 50 m^3) rockfalls and rockslides occurred (Fig. 5b). A cluster of negative changes that is registered at the central part of the rockwall can be traced back to errors in the photogrammetric model of 5-Jul-2012 since it appears as a positive change during the subsequent period (compare Fig. 5b,c). The overall loss at the rockwall is consistent with the LiDAR-based estimates; the limited MVS coverage at the base of the scarp only permits to establish a lower bound for the sediment outwash from the scree slopes (Fig. 5b).

The subsequent period (~5 months, autumn to spring) is characterized by an important activity comprising major rockfalls, rockslides and accumulation of scree at the base of the scarp. (Fig. 5c). A major rockslide at the western part of the rockwall released a volume of 2.17×10^3 ± 320 m^3. The high magnitude of changes is consistent with a prolonged winter and higher snow accumulation than the average values observed in the last 10 years resulting in extensive freeze-thaw cycles and a large volume of snowmelt water in early spring.

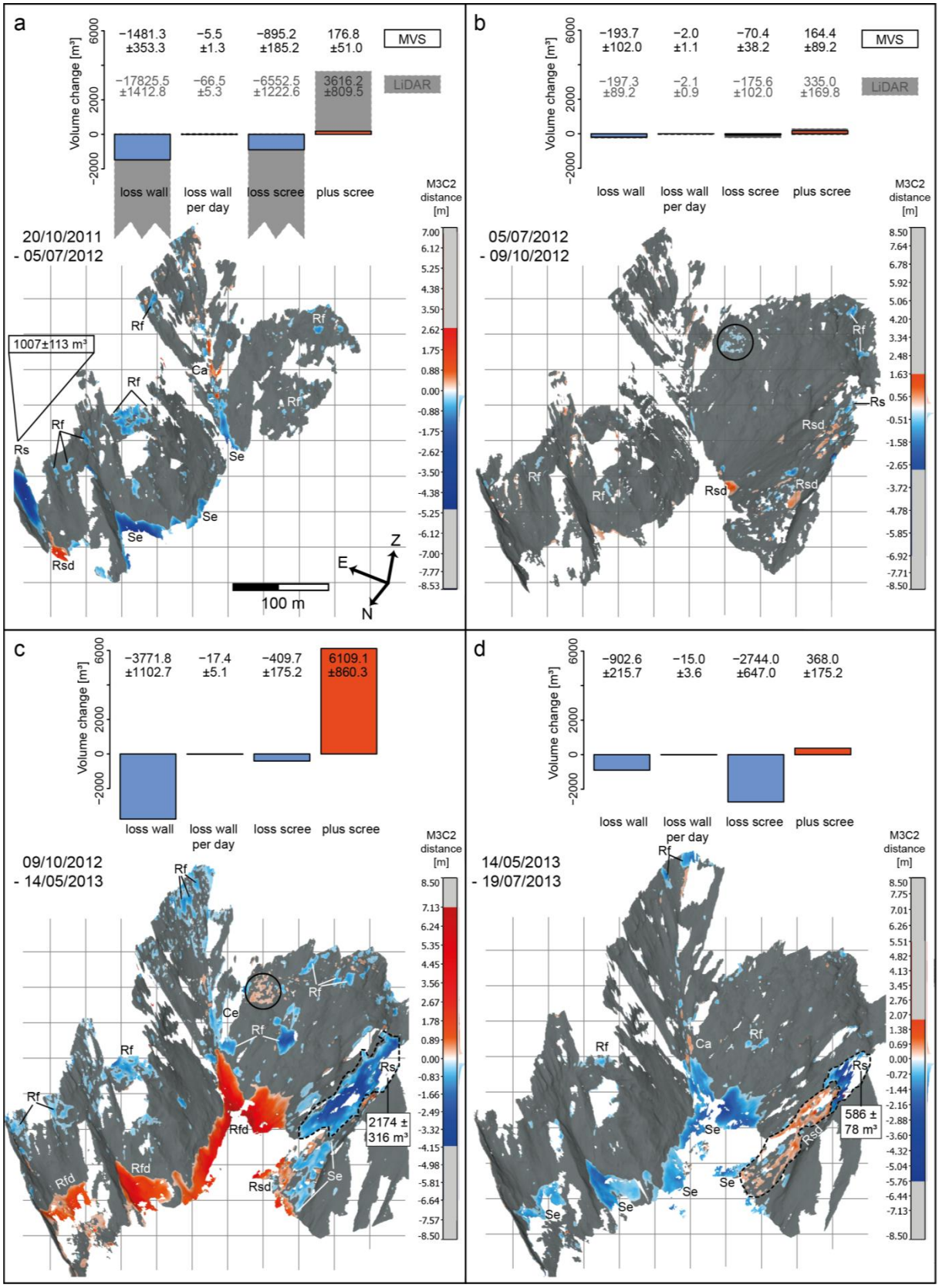
a
Volume change [m³]
6000
2000
0
−2000
−1481.3 ±353.3
−5.5 ±1.3
−895.2 ±185.2
176.8 ±51.0
MVS
−17825.5 ±1412.8
−66.5 ±5.3
−6552.5 ±1222.6
3616.2 ±809.5
LiDAR
loss wall
loss wall per day
loss scree
plus scree
M3C2 distance [m]
7.00
6.12
5.25
4.38
3.50
2.62
1.75
0.88
0.00
-0.88
-1.75
-2.62
-3.50
-4.38
-5.25
-6.12
-7.00
-7.77
-8.53
20/10/2011 - 05/07/2012
1007±113 m³
Rf
Ca
Rs
Se
Rsd
100 m
Z
E
N
b
−193.7 ±102.0
−2.0 ±1.1
−70.4 ±38.2
164.4 ±89.2
−197.3 ±89.2
−2.1 ±0.9
−175.6 ±102.0
335.0 ±169.8
8.50
7.64
6.78
5.92
5.06
4.20
3.34
2.48
1.63
0.56
-0.51
-1.58
-2.65
-3.72
-4.78
-5.85
-6.92
-7.71
-8.50
05/07/2012 - 09/10/2012
Rf
Rs
Rsd
c
−3771.8 ±1102.7
−17.4 ±5.1
−409.7 ±175.2
6109.1 ±860.3
8.50
7.13
6.24
5.35
4.45
3.56
2.67
1.78
0.89
0.00
-0.83
-1.66
-2.49
-3.32
-4.15
-4.98
-5.81
-6.64
-7.57
-8.50
09/10/2012 - 14/05/2013
Rf
Ce
Rfd
Rsd
Se
2174 ± 316 m³
d
−902.6 ±215.7
−15.0 ±3.6
−2744.0 ±647.0
368.0 ±175.2
8.50
7.75
7.01
6.26
5.51
4.82
4.13
3.45
2.76
2.07
1.38
0.69
0.00
-0.72
-1.44
-2.16
-2.88
-3.60
-4.32
-5.04
-5.76
-6.44
-7.13
-8.50
14/05/2013 - 19/07/2013
Rf
Ca
Rs
Se
586 ± 78 m³

Fig. 5. Detected changes at the Super-Sauze main scarp for the period 2011–2013, volume balances and geomorphological interpretation. (a) 20-Oct-2011 till 5-Jul-2012, (b) 5-Jul-2012 till 9-Oct-2012, (c) 9-Oct-2012 till 14-May-2013, and (d) 14-May-2013 till 19-Jul-2013. The abbreviations indicate zones of rockfalls (Rf), rockslides (Rs), rockfall- and rockslide deposits (Rfd and Rsd), outwash of the scree slopes at the base of the scarp (Se), and accumulation or outwash within the channel (Ca/Ce) in the centre of the scarp. The black circle marks a cluster of false positive detections resulting from reconstruction errors.

The last period (~2 months, summer–autumn) was again dominated by outwash at the scree slopes. The rockslide zone at the western part of the scarp, which was activated during the previous time interval, still shows an important activity (580 ± 320 m^3; Fig. 5d). Some small-size rockfall events (< 50 m^3) distributed all along the scarp were also detected.

In summary, the change detection provides a detailed picture of the surface evolution and main processes controlling the dynamics of the main scarp. Residual false detections can be excluded through the interpretation of subsequent periods. At a confidence interval of 95%, false positive detection can be largely avoided and the overall accuracy of the surface reconstruction (*RMSE* in range of 3–6 cm) allows the detection of changes exceeding 20 cm. For individual medium and large size rockfalls and rockslides (> 500 m^3), the estimated volumes are approximately 5% lower than those based on LiDAR.

In order to estimate the average erosion rate at the main scarp for the studied period, change detection is performed between the ALS of 20-Oct-2011 and the photogrammetric model of 19-07-2013. The total volume loss for this period is $22.57\times10^3 \pm 1.99\times10^3$ m^3. With regard to the surface area where both point clouds of the rock wall overlap (51.25×10^3 m^2) this corresponds to an average erosion rate of 24.8 ± 2.2 cm m^{-2} yr^{-1}. This is a conservative estimate since changes below 0.2 m could not be detected at 95% confidence. Nevertheless, it exceeds by a factor of 40 the average erosion rates reported for badlands in the Southern French Alps with very similar rock types and topography (Saez

et al., 2011). This is because erosion in these badlands is mainly driven by freeze–thaw and wetting–drying cycles producing regolith at a much slower rate than the gravitational failures at the investigated landslide scarp. Considering a unit weight of 16.6– 17.1 kN m^{-3} (Maquaire et al., 2003) the main scarp delivered in total $38.89\times10^3 \pm 3.99\times10^3$ t of sediment in less than three years which corresponds to a sediment yield of 426.9 ± 43.9 kg m^{-2} yr^{-1}. In comparison long term rates of 19 kg m^{-2} yr^{-1} have been reported for slow-moving landslides in the Eel River catchment, California, over a period of 62 years (Mackey and Roering, 2011). Among many environmental factors that may contribute to the great difference in the sediment yield, our results are representative for a 2.5 years period at the main scarp of one specific landslide and may represent the record of a very active phase compared to the long-term average. In addition, Mackey and Roering (2011) report the sediment delivery rate at the toe of the landslides, while the quantities provided here represent what is released at the main scarp. This also includes sediments that, once released, may bypass the slow flow-like transport to the toe (e.g. direct fluvial transport).

In any case, these figures show that the investigated landslide scarp is an important point-source of loose sediments. The latter are delivered effectively through the main landslide body (Section 4.3.2) into the channels, and therefore should be considered as a significant term in the sediment budgets at the catchment scale.

4.3.2 Deformation of the landslide: quantification and interpretation

According to the residual errors between photogrammetric models and the ALS model of the entire landslide (Table 5), a co-registration error of 0.20 m is used for the computation of the confidence interval during the change detection for the entire landslide. In order to capture the cumulative displacement and volume changes, three analyses were carried out: 1) between the ALS point cloud of 29-Aug-2012 and the MVS point cloud of 10-Oct-2012 (42 days), 2) between the two MVS point

clouds of 10-Oct-2012 and 19-Jul-2013 (282 days), and 3) between the ALS point cloud of 29-Aug-2012 and the MVS point cloud of 19-Jul-2013 (324 days).

At an estimated co-registration error of 0.2 m, the minimum displacement that can be detected at a 95% confidence level is 0.4 m. The maximum measured change over the 324 days monitoring period varied between -6.8 and 6.8 m; important displacement of almost the entire landslide, a major rockfall at the rockwall and the corresponding material accumulation at the base of the main scarp were depicted (Fig. 6a,b). Interestingly, the upper part of the landslide remained largely stable, whereas a secondary scarp formed further downslope and currently delineates the most active part of the landslide. The secondary scarp was already activated during the first 42 days (Fig. 6a) and a rather localised displacement of material induced surface changes between −3.6 and 2.3 m. Minor detected changes include small rockfalls (< 100 m^3) and scree accumulation at the main scarp as well as traces of a translational failure in the central part of the landslide body (Fig. 6c). A few zones with false detection areas are indicated in Fig. 6a,b. Due to constrain on the viewing geometry, these areas were imaged from large distances and relatively oblique incidence angles (<30˚) at which fine structures such as thalwegs and gullies cannot be reconstructed correctly. To address this issue, dedicated images for these error prone areas were acquired for the other date (19-Jul-2013) and enabled us to reduce the amount of artifacts.

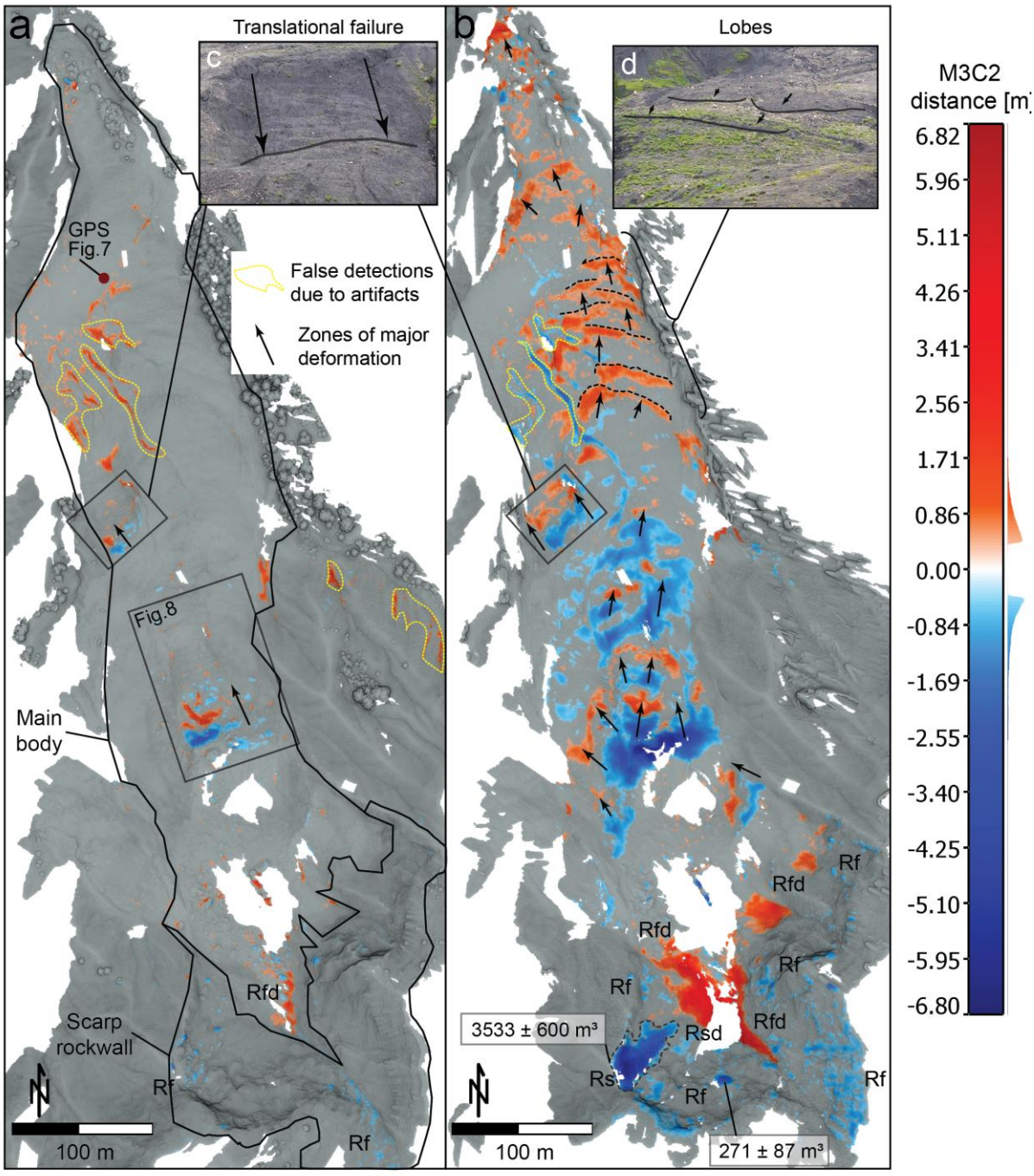
a
Translational failure
c
GPS
Fig.7
False detections
due to artifacts
Zones of major
deformation
Fig.8
Main
body
Rfd
Scarp
rockwall
Rf
Rf
100 m
b
Lobes
d
Rf
Rfd
Rfd
Rf
Rf
3533 ± 600 m³
Rfd
Rsd
Rs
Rf
Rf
271 ± 87 m³
100 m
M3C2
distance [m]
6.82
5.96
5.11
4.26
3.41
2.56
1.71
0.86
0.00
-0.84
-1.69
-2.55
-3.40
-4.25
-5.10
-5.95
-6.80

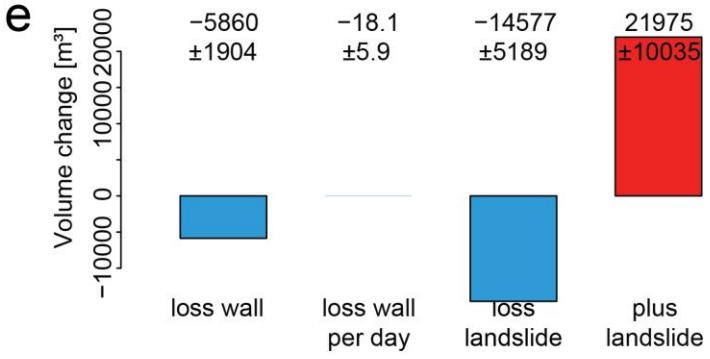
e
Volume change [m³]
−10000
0
10000
20000
−5860
±1904
−18.1
±5.9
−14577
±5189
21975
±10035
loss wall
loss wall
per day
loss
landslide
plus
landslide

Fig. 6. Detected changes at the Super-Sauze landslide body and main scarp for the period 2012–2013 in terms of volume balances and geomorphological interpretation. (a) 29-Aug-2012 till 10-Oct-2012. (b) 10-Oct-2012 till 19-Jul-2013. The abbreviations indicate zones with rockfalls (Rf), rockslides (Rs), rockfall- and rockslide deposits (Rfd, Rsd), and gully erosion (Ge). Bright dotted lines outline zones with false detections. (c) Photograph captured on 19-07-2013 indicating the translation failure that evolved during the surveyed period. (d) Photograph captured on 19-Jul-2013 highlighting the lobes that progressed downslope during the period 10-Oct-2012 till 19-Jul-2013. (e) Volume budgets for the complete period 29-Aug-2012 till 19-Jul-2013.

The activity at the secondary scarp increased in the 282 days period between 10-Oct-2012 and 19-Jul-2013. The general change pattern indicates a strong displacement from the central part of the landslide (mainly negative distances) towards the lower part (mainly positive distances, Fig. 6b). Notable features include the progression of the previously triggered translational failure (Fig. 6c), lobes that display a flow-like downslope movement (Fig. 6d) and a significant advancement of the landslide toe. The depicted rockfalls at the rockwall resemble the results of the change detection at the main scarp (Fig. 5c,d). The volumes released from two source areas are estimated as 270 ± 90 m^3 and 3.53×10^3 ± 600 m^3 (Fig. 6b), which is consistent with the estimates from the main scarp models for the same areas and time periods (250 ± 50 m^3 and 3.12×10^3 ± 510 m^3, respectively).

Among the detected changes, we distinguish three main components: 1) volume loss at the rockwall, 2) volume gains of the landslide body (including gains at the scree slopes at the base of the main scarp) and, 3) volume loss of the landslide body. The total volume budget (Fig. 6e) of the landslide body comprises a loss of $14.58\times10^3 \pm 5.19\times10^3$ m^3 and a gain of $21.98\times10^3 \pm 10.04\times10^3$ m^3. Considering the large overlap in the confidence intervals of both quantities, no significant total volume change has taken place in the surveyed time period. This shows that the loose sediment generated at the scarp is transported effectively into the channels.

Artifacts in the MVS model of 10-Oct-2012 hindered to fully track the evolution of deeply incised gullies at the central part of the landslide for the two sub-periods (Fig. 6a,b). However, the reconstruction of the respective area could be significantly enhanced in the photogrammetric model of 19-Jul-2013. Change detection between the latter and the airborne LiDAR point cloud of 29-Aug-2012 (essentially the sum of the changes shown in Fig. 6a,b) indicates an incision of the central gully of up to 0.8 m. Besides the flow-like surface deformation features, torrential transport in the gullies constitutes an important mechanism for sediment transfer through the landslide body and into the adjacent channels.

The general pattern of the observed movement is consistent with previous studies of the landslide dynamics (Malet et al., 2002; Travelletti et al., 2012). However, due to the flow-like behavior of the landslide, the largest component of the 3D displacement is typically parallel to the slope and hence an important component of the displacement is not comprised in the distances measured normal to the surfaces. To illustrate the possibility to quantify the 3D dispalcement, vectors are calculated for two sub-areas (Fig. 6) being located 1) downslope of the secondary scarp, and 2) at the landslide toe where a comparison with a permanent GPS station installed on the landslide is possible.

To measure 3D displacement at the exact position of the GPS, the corresponding points in the ALS point clouds were aligned manually (simple translation) to the position of the GPS as depicted in the MVS point clouds. The same procedure was performed for points on a pillar with solar panels next to the GPS. Displacement vectors are obtained from the point coordinates before and after the transforms. The results are shown in Fig. 7 indicating a total displacement of 3.62 m measured among the different point clouds, whereas the permanent GPS indicates a total displacement of 3.15 m. The difference of 0.47 m accumulates errors in the absolute geolocation, the co-registration of the point clouds, and errors induced by the matching process. The residual georeferencing error of the MVS model for 19-Jul-2013 is only 0.05 ± 0.04 m and the relative *RMSE* value over stable areas after alignment is 0.17 m as a maximum. To understand the comparatively high error of the displacement

measurement, it is important to note that fine structures such as the GPS station are generally over-generalized due to the regularization in the photogrammetric modelling. This was especially true for the model of 10-Oct-2012 in which the GPS position was imaged from a relatively remote position (~ 700 m) and explains the greater deviation for the period 29-Aug-2012 to 10-Oct-2012. Thus the relative error of 0.47 m can be considered as an upper bound for the displacement estimates for the central most active part where matching was performed on well-defined boulders using the ICP algorithm for fine registration.

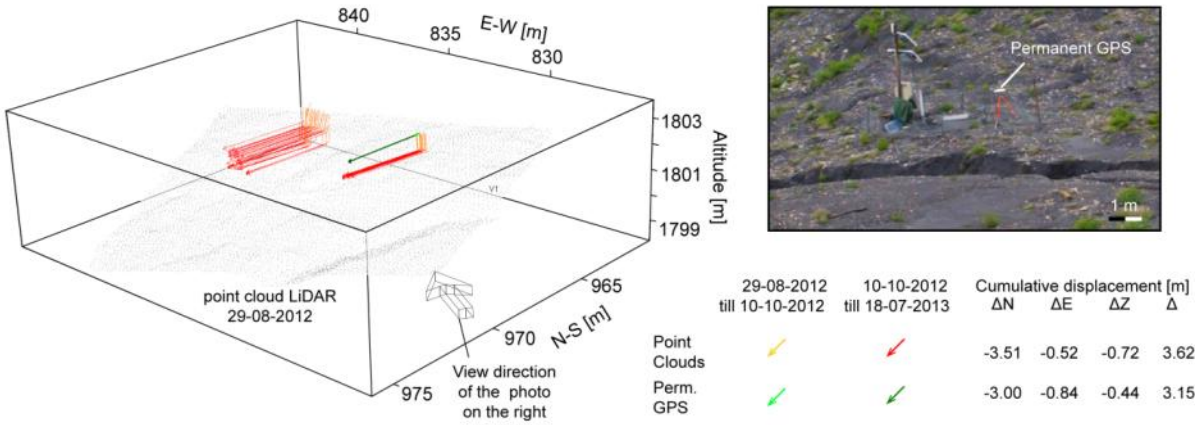

Fig. 7. 3D displacement vectors measured via point matching among the different point clouds and a comparison with permanent GPS measurements.

The 3D displacement measurements for the central part of the landslide were obtained through a piecewise alignment (translation and rotation) of rigid blocks that could be identified in at least two of the three point clouds. The ICP algorithm was used for fine registration, whereas if the distances were larger than 1 m an initial guess for the translational component was provided manually. The measurements for the period 29-Aug-2012 to 10-Oct-2012 suggest a maximum displacement of 5.79 m with at most 4.53 m in the Z-component and 4.01 m in the horizontal (E–W and N–S) component (Fig. 8a). The spatial pattern of displacement is consistent with satellite-based measurements covering nearly the same time period (Stumpf et al., 2014). However, the maximum

horizontal displacement of 4.01 m could not be depicted with spaceborne measurement due to low correlation in areas with high deformation.

During the second period (10-Oct-2012 to 19-Jul-2013), the displacement increased up to 25.55 m with a maximum 22.76 m in the horizontal component and a maximum of 11.82 m in the Z-component (Fig. 8b). On average, displacement rates of maximal 14 cm d^{-1} for the time between late August and early September 2012, and of maximal 9 cm d^{-1} for the following months until mid-July of the next year are estimated. A meaningful interpretation these figures, however, must consider that the displacement rates are highly variable in time with a significant decrease in the winter months and an increase in the spring months (Amitrano et al., 2007). It is, therefore, likely that the displacement rates in spring 2013 were significantly higher than the observed average maximum of 9 cm d^{-1}.

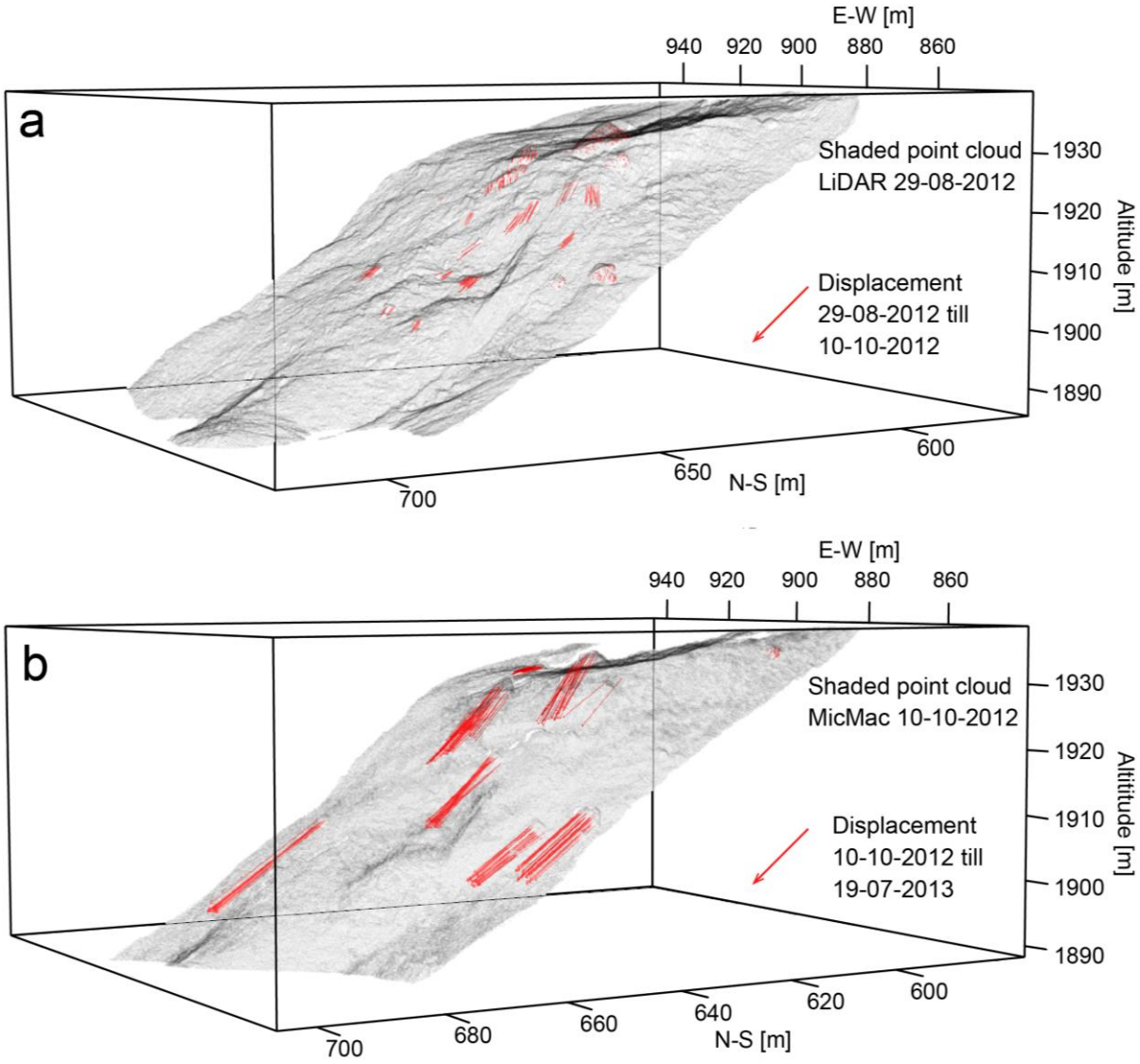

Fig. 8. 3D displacement vectors measured on rigid structures with the ICP method between (a) the ALS of 29-Aug-2012 and the MVS point cloud of 10-Oct-2012, and (b) the MVS point cloud of 10-Oct-2012 and 19-Jul-2013. (c) Terrestrial photograph indicating the subset of analysed area (white dashed line).

4.4 Potential and limitations of terrestrial SfM-MVS for landslide monitoring

Similar to several previous studies (see Section 2), we found that SfM-MVS should be considered as an accurate and cost-effective technique to obtain 3D information on geomorphological processes. The use of several open-source SfM-MVS pipelines was evaluated for landslide monitoring and it was demonstrated that a MicMac-based pipeline can provide accuracies and coverage which approach the quality of terrestrial and airborne LiDAR point clouds if the geometry of the image acquisition is well adapted to the surveyed object. While James and Robson (2012) suggested a relative precision of 1:1000 (*RMSE* of 1 m at imaging distance of 1000 m) of SfM-MVS, our findings suggest that a relative precision of 1:500 and better is possible. We found that the quality of the surface reconstruction degrades significantly when incidence angles exceed 30º, and an accuracy of a few centimeters could only be obtained at close ranges up to 200 m. While the use of a larger focal length can enhance the resolution at greater imaging distances, the number of required photographs will increase linear with the focal length to obtain the same coverage. A further issue is that the perspective distortion decreases at a greater focal length which leads to a stronger ambiguity regarding the depth of the scene.

Using the M3C2 algorithm for change detection analysis allowed us to take into account the quantified errors, establishing a 95% confidence for reliable detection of changes above 20 cm at the main scarp and above 40 cm at the scale of the entire landslide. Remaining outliers could be traced back to local artifacts in the 3D reconstruction and excluded from the analysis. 3D displacement measurements at the location of a permanent GPS station suggested a maximum error of 0.47 m.

Estimated rockfall volumes differed by 4% from the respective volumes calculated from terrestrial LiDAR.

Despite these encouraging results and a high degree of automation, several potential pitfalls deserve further consideration since they may increase the need for manual intervention in the pipeline and compromise the accuracy. A non-trivial aspect of terrestrial MVS in complex natural landscapes is the planning of the acquisition geometry. Practical guidelines for acquisition planning with buildings, indoor spaces and cultural objects can be found in (Luca et al., 2013; Wenzel et al., 2013) but it remains difficult to provide general rules for natural terrain. Smaller base-to-height ratios (i.e. short distances between neighboring views) diminish the accuracy of the surface reconstruction, while larger baselines complicate the matching. The MicMac library includes a tool for image selection and an overly dense linear network is preferable to avoid unconnected image clusters. The angle between neighboring views must not exceed 15˚ and their overlap should be greater 80%. Motion blurs and changes in the lens parameters (e.g. auto-focus) should be avoided. The surveys were conducted under variable weather conditions ranging from bright sunshine to light rain. However, diffused lighting (i.e. clouded sky) is ideal to avoid effects from moving shadows and low contrast in very bright or very dark areas. Each part of the surface should be visible in three to six well separated views including ideally one view directed close to perpendicular to the surface. If these conditions are satisfied, accuracies approaching LiDAR quality can be expected, while the costs, logistics and time requirements for the data acquisitions are significant lower. In this context, it is noteworthy that the acquisitions of the photographs at the main scarp could be carried out in approximately 30 min, while half a day was needed to obtain 400 images covering the entire landslide. Depending on the processing chain, the reconstruction required 2–3 days on a desktop workstation with 8 cores and 32 GB RAM. While the MicMac based pipeline is the slowest among the tested techniques, it is less demanding in terms of memory consumption.

For the landslide terrain investigated in this study, views perpendicular to the surface could not be obtained for all positions and many of the remaining artifacts must be attributed to these issues. At

sites where the terrain is unfavorable for terrestrial imaging perpendicular to the surface, alternative platforms such as UAVs (Niethammer et al., 2011; Lisein et al., 2013) should be considered.

To fully understand the constraints of a specific site, it is generally recommendable to conduct at least one preliminary survey to optimize the protocol for operational monitoring. For future operational monitoring at the investigated landslide, it is recommended to integrate the acquisition protocols for the main scarp and the landslide body (~500 images) to avoid multiple processing chains. Tools for the optimization of the camera network based on preliminary video acquisitions have been recently proposed (Alsadik et al., 2013) and should be tested for the optimization of acquisition geometry in natural terrain. A further option could be near-real-time user interaction to determine the next best viewing position (e.g. Hoppe et al., 2012), which however requires a direct downlink from the camera to a computer and might not be easy to implement in the field.

A general limitation of landslide monitoring with passive optical sensors is the inability to penetrate vegetation. The reconstructed surfaces over vegetated areas represent an average canopy surface, and due to high surface roughness and random pattern they generally incur large errors. The Super-Sauze landslide is very sparsely vegetated and the manual removal of few vegetated areas was straightforward. For more complex settings, an automated point cloud classification with dedicated tools (Brodu and Lague, 2012) might be desirable. In SfM-MVS point clouds, the vertical structure of the vegetation is represented much poorer than in LiDAR point clouds, whereas RGB color information that can be mapped automatically to all 3D point provides useful additional features.

Regarding the georeferencing, we found GCP-based referencing with photogrammetric targets during the SfM phase to be a more convenient strategy than establishing point-to-point correspondence after dense matching. In cases of limited GPS accuracy, the ICP algorithm proved to be a valuable tool to resolve residual alignment errors (translation and rotation). An intermediate solution for small and medium sized objects (e.g. the main scarp) would be to resolve the model scale with a scale bar that must be visible in at least two images and recover translation and rotation through matching of the dense point clouds of stable terrain. In any case, it is indispensable for the alignment to include a

sufficiently large proportion of stable and vegetation-free terrain within the reconstruction, which should be kept in mind during the image acquisition. For the validation of displacement rates, we recommend measurements at clearly visible photogrammetric targets rather than GPS antenna.

5. Conclusion

This study investigated the use of SfM and MVS pipelines for the terrestrial monitoring of landslides. In a comparative assessment of different open-source solutions the MicMac library yielded the more accurate results, whereas VisualSfM and PMVS permitted a higher degree of automation. Compared to LiDAR point clouds, *RMSE* of the photogrammetric point clouds generally did not exceed 0.2 m for the reconstruction of the entire landslide and 0.06 m for the reconstruction of the main scarp. The M3C2 algorithm was found to be a versatile and accurate tool for the reliable detection of changes and the possibility to obtain volumes, erosion rates and 3D displacement estimates was illustrated for especially active zones. It could be demonstrated that at the slope scale terrestrial multi-view photogrammetry is sufficiently accurate to detect surface changes in the range of decimeters. Thus, the technique currently remains less precise than TLS or GPS but provides spatially distributed information at significant lower costs and is, therefore, valuable for many practical landslide investigations.

An option that has not been explored in this study is the possibility to measure 3D displacement from temporal sequence of stereo-pairs which is a technique frequently used in solid mechanics (Sutton et al., 2009). The determination of 3D vectors through matching in the image space can be expected to provide more precise results than matching of the resulting point clouds. More frequent acquisitions might be required in this context to avoid temporal decorrelation. The planning and optimization of the image acquisition protocols still remains challenging in complex natural terrain and further research is needed to establish tools that enable a more straightforward optimization of the camera network for operational monitoring.

Acknowledgements

This work was supported by the project SafeLand '*Living with landslide risk in Europe: assessment, effects of global change, and risk management strategies*' (Grant Agreement No. 226479) funded by the 7th Framework Programme of the European Commission and the project FOSTER '*Spatio-temporal data mining: application to the understanding and monitoring of soil erosion*' funded by the French Research Agency (Contract ANR Cosinus, 2011–2013). The ALS dataset was acquired through the project '*Landslide early-warning*' funded by the EUR-OPA Major Hazards Open Partial Agreement of Council of Europe. The GNSS data are provided by the French Landslide Observatory (OMIV: Observatoire Multidisciplinaire des Instabilités de Versants: http://omiv.unistra.fr).

References

Abellán, A., Oppikofer, T., Jaboyedoff, M., Rosser, N.J., Lim, M., Lato, M.J., 2013. Terrestrial laser scanning of rock slope instabilities. Earth Surface Processes and Landforms, 48.

Alsadik, B., Gerke, M., Vosselman, G., 2013. Automated camera network design for 3D modeling of cultural heritage objects. Journal of Cultural Heritage, 14(6).

Amitrano, D., Gaffet, S., Malet, J.-P., Maquaire, O., 2007. Understanding mudslides through micro-seismic monitoring: the Super-Sauze (South-East French Alps) case study. Bulletin de la Societe Geologique de France, 178(2), 149-157.

Aryal, A., Brooks, B.A., Reid, M.E., Bawden, G.W., Pawlak, G.R., 2012. Displacement fields from point cloud data: Application of particle imaging velocimetry to landslide geodesy. Journal of Geophysical Research: Earth Surface, 117(F1), F01029.

Barnhart, T., Crosby, B., 2013. Comparing Two Methods of Surface Change Detection on an Evolving Thermokarst Using High-Temporal-Frequency Terrestrial Laser Scanning, Selawik River, Alaska. Remote Sensing, 5(6), 2813-2837.

Bretar, F., Arab-Sedze, M., Champion, J., Pierrot-Deseilligny, M., Heggy, E., Jacquemoud, S., 2013. An advanced photogrammetric method to measure surface roughness: Application to volcanic terrains in the Piton de la Fournaise, Reunion Island. Remote Sensing of Environment, 135(0), 1-11.

Brodu, N., Lague, D., 2012. 3D terrestrial lidar data classification of complex natural scenes using a multi-scale dimensionality criterion: Applications in geomorphology. ISPRS Journal of Photogrammetry and Remote Sensing, 68(0), 121-134.

Cignoni, P., Callieri, M., Corsini, M., Dellepiane, M., Ganovelli, F., Ranzuglia, G., 2008. Meshlab: an open-source mesh processing tool, Eurographics Italian Chapter Conference. The Eurographics Association, pp. 129-136.

Dandois, J.P., Ellis, E.C., 2010. Remote Sensing of Vegetation Structure Using Computer Vision. Remote Sensing, 2(4), 1157-1176.

Deseilligny, M.-P., Belveaux, J., Choqueux, G., Deveau, M., Girod, L., 2013. MicMac, Apero and Other Beverages in a Nutshell, ENSG - Marne-la-Vallée, pp. 275.

Deseilligny, M.P., Clery, I., 2011. Apero, an open source bundle adjusment software for automatic calibration and orientation of set of images. In: F. Remondino, S. El-Hakim (Eds.), 4th ISPRS International Workshop 3D-ARCH 2011: ″3D Virtual Reconstruction and Visualization of Complex Architectures″, Trento, Italy, pp. 269-276.

EDF-R&D, TelecomParisTech, 2013. CloudCompare (version 2.5) [GPL software]. Retrieved from http://www.danielgm.net/cc/, [last access: 21/10/2013].

Flageollet, J.-C., Maquaire, O., Martin, B., Weber, D., 1999. Landslides and climatic conditions in the Barcelonnette and Vars basins (Southern French Alps, France). Geomorphology, 30(1-2), 65-78.

Fonstad, M.A., Dietrich, J.T., Courville, B.C., Jensen, J.L., Carbonneau, P.E., 2013. Topographic structure from motion: a new development in photogrammetric measurement. Earth Surface Processes and Landforms, 38(4), 421-430.

Fraser, C.S., 1997. Digital camera self-calibration. ISPRS Journal of Photogrammetry and Remote Sensing, 52(4), 149-159.

Fryer, J., Mitchell, H., Chandler, J., 2007. Applications of 3D Measurement from Images. Whittles Publishing, Caithness, Scotland.

Furukawa, Y., Curless, B., Seitz, S.M., Szeliski, R., 2010. Towards Internet-scale multi-view stereo, IEEE Conference on Computer Vision and Pattern Recognition, pp. 1434-1441.

Furukawa, Y., Ponce, J., 2010. Accurate, Dense, and Robust Multiview Stereopsis. Pattern Analysis and Machine Intelligence, IEEE Transactions on, 32(8), 1362-1376.

Gance, J., Malet, J.P., Dewez, T., Travelletti, J., 2014. Target Detection and Tracking of moving objects for characterizing landslide displacements from time-lapse terrestrial optical images. Engineering Geology, 172(0), 26-40.

Girardeau-Montaut, D., Roux, M., Marc, R., Thibault, G., 2005. Change detection on points cloud data acquired with a ground laser scanner. International Archives of Photogrammetry, Remote Sensing and Spatial Information Sciences, 36(part 3), W19.

Gómez-Gutiérrez, Á., Schnabel, S., Berenguer-Sempere, F., Lavado-Contador, F., Rubio-Delgado, J., 2014. Using 3D photo-reconstruction methods to estimate gully headcut erosion. CATENA, 120(0), 91-101.

Hartley, R.I., Zisserman, A., 2004 Multiple View Geometry in Computer Vision, Second. Cambridge University Press.

Henry, J.-B., Malet, J.-P., Maquaire, O., Grussenmeyer, P., 2002. The Use of Small-Format and Low-Altitude Aerial Photos for the Realization of High-Resolution DEMs in Mountainous Areas: Application to the Super-Sauze Earthflow (Alpes-De-Haute-Provence, France). Earth Surface Processes and Landforms, 27, 1339–1350.

Heritage, G.L., Large, A.R.G., 2009. Laser scanning for the environmental sciences. Wiley-Blackwell, London.

Hirschmuller, H., 2008. Stereo Processing by Semiglobal Matching and Mutual Information. IEEE Transaction on Pattern Analysis and Machine Intelligence, 30(2), 328-341.

Hoppe, C., Klopschitz, M., Rumpler, M., Wendel, A., Kluckner, S., Bischof, H., Reitmayr, G., 2012. Online Feedback for Structure-from-Motion Image Acquisition, Vritish Machine Vision Conference, Guildford, UK, pp. 1-12.

Hovius, N., Stark, C.P., Hao-Tsu, C., Jiun-Chuan, L., 2000. Supply and removal of sediment in a landslide-dominated mountain belt: Central Range, Taiwan. The Journal of Geology, 108(1), 73-89.

Innovmetric, 2010. PolyWorks User's Manual - 3-D scanner and 3-D digitizer software from InnovMetric Software Inc. http://www.innovmetric.com/, [last access: 21/10/2013].

Jaboyedoff, M., Oppikofer, T., Abellán, A., Derron, M.-H., Loye, A., Metzger, R., Pedrazzini, A., 2010. Use of LIDAR in landslide investigations: a review. Natural Hazards, 1-24.

James, M.R., Robson, S., 2012. Straightforward reconstruction of 3D surfaces and topography with a camera: Accuracy and geoscience application. Journal of Geophysical Research, 117(F3), F03017.

James, M.R., Varley, N., 2012. Identification of structural controls in an active lava dome with high resolution DEMs: Volcán de Colima, Mexico. Geophysical Research Letters, 39(22), L22303.

Javernick, L., Brasington, J., Caruso, B., 2014. Modeling the topography of shallow braided rivers using Structure-from-Motion photogrammetry. Geomorphology, 213(0), 166-182.

Kääb, A., Girod, L., Berthling, I., 2013. Surface kinematics of periglacial sorted circles using Structure-from-Motion technology. The Cryosphere Discuss., 7(6), 6043-6074.

Kazhdan, M., Hoppe, H., 2013. Screened poisson surface reconstruction. ACM Transactions on Graphics (TOG), 32(3), 29.

Lague, D., Brodu, N., Leroux, J., 2013. Accurate 3D comparison of complex topography with terrestrial laser scanner: Application to the Rangitikei canyon (N-Z). ISPRS Journal of Photogrammetry and Remote Sensing, 82(0), 10-26.

Lisein, J., Pierrot-Deseilligny, M., Bonnet, S., Lejeune, P., 2013. A Photogrammetric Workflow for the Creation of a Forest Canopy Height Model from Small Unmanned Aerial System Imagery. Forests, 4(4), 922-944.

Lowe, D.G., 2004. Distinctive Image Features from Scale-Invariant Keypoints. International Journal of Computer Vision, 60(2), 91-110.

Luca, L.D., Pierrot-Deseilligny, M., Remondino, F., Beninstant, P., Cléry, I., Lombardo, J., Nex, F., Nony, N., 2013. Tapenade - Tools and Acquisition Protocols for Enancing Artifacts Documentation, http://www.tapenade.gamsau.archi.fr/TAPEnADe/Protocols.html, [last access: 05-10-2013].

Lucieer, A., Jong, S.M.d., Turner, D., 2014. Mapping landslide displacements using Structure from Motion (SfM) and image correlation of multi-temporal UAV photography. Progress in Physical Geography, 38(1), 97-116.

Mackey, B.H., Roering, J.J., 2011. Sediment yield, spatial characteristics, and the long-term evolution of active earthflows determined from airborne LiDAR and historical aerial photographs, Eel River, California. Geological Society of America Bulletin, 123(7-8), 1560-1576.

Malet, J.P., Maquaire, O., Calais, E., 2002. The use of Global Positioning System techniques for the continuous monitoring of landslides: application to the Super-Sauze earthflow (Alpes-de-Haute-Provence, France). Geomorphology, 43(1-2), 33-54.

Maquaire, O., Malet, J.-P., Remaıtre, A., Locat, J., Klotz, S., Guillon, J., 2003. Instability conditions of marly hillslopes: towards landsliding or gullying? The case of the Barcelonnette Basin, South East France. Engineering Geology, 70(1), 109-130.

Monserrat, O., Crosetto, M., 2008. Deformation measurement using terrestrial laser scanning data and least squares 3D surface matching. ISPRS J Photogramm Remote Sens, 63, 142–154.

Niethammer, U., James, M.R., Rothmund, S., Travelletti, J., Joswig, M., 2011. UAV-based remote sensing of the Super-Sauze landslide: Evaluation and results. Engineering Geology, 128(9), 2–11.

Ouédraogo, M.M., Degré, A., Debouche, C., Lisein, J., 2014. The evaluation of unmanned aerial system-based photogrammetry and terrestrial laser scanning to generate DEMs of agricultural watersheds. Geomorphology, 214(0), 339-355.

Pierrot-Deseilligny, M., Paparoditis, N., 2006. A Multiresolution and Optimization-Based Image Matching Approach : An Application to Surface Reconstruction from Spot 5-HRS Stereo Imagery, WG I/5 & I/6 Workshop on Topographic Mapping from Space (with Special Emphasis on Small Satellites), Ankara, Turkey.

Pollefeys, M., Koch, R., Gool, L., 1999. Self-Calibration and Metric Reconstruction Inspite of Varying and Unknown Intrinsic Camera Parameters. International Journal of Computer Vision, 32(1), 7-25.

Remondino, F., Pizzo, S., Kersten, T., Troisi, S., 2012. Low-Cost and Open-Source Solutions for Automated Image Orientation – A Critical Overview. In: M. Ioannides, D. Fritsch, J. Leissner, R. Davies, F. Remondino, R. Caffo (Eds.), Progress in Cultural Heritage Preservation. Lecture Notes in Computer Science. Springer Berlin Heidelberg, pp. 40-54.

Rothermel, M., Wenzel, K., Fritsch, D., Haala, N., 2012. SURE: Photogrammetric Surface Reconstruction from Imagery, LC3D Workshop, Berlin, Germany.

Saez, J.L., Corona, C., Stoffel, M., Rovéra, G., Astrade, L., Berger, F., 2011. Mapping of erosion rates in marly badlands based on a coupling of anatomical changes in exposed roots with slope maps derived from LiDAR data. Earth Surface Processes and Landforms, 36(9), 1162-1171.

Seitz, S.M., Curless, B., Diebel, J., Scharstein, D., Szeliski, R., 2006. A Comparison and Evaluation of Multi-View Stereo Reconstruction Algorithms, Computer Vision and Pattern Recognition, 2006 IEEE Computer Society Conference on, pp. 519-528.

Snavely, N., Seitz, S., Szeliski, R., 2008. Modeling the World from Internet Photo Collections. International Journal of Computer Vision, 80(2), 189-210.

Strecha, C., Von Hansen, W., Van Gool, L., Fua, P., Thoennessen, U., 2008. On benchmarking camera calibration and multi-view stereo for high resolution imagery, Computer Vision and Pattern Recognition, 2008. CVPR 2008. IEEE Conference on, pp. 1-8.

Stumpf, A., Malet, J.-P., Allemand, P., Ullrich, P., 2014. Surface reconstruction and landslide displacement monitoring with Pléiades VHR satellite images. ISPRS Journal of Photogrammetry and Remote Sensing, 95, 1–12.

Stumpf, A., Malet, J.-P., Kerle, N., Niethammer, U., Rothmund, S., 2013. Image-based mapping of surface fissures for the investigation of landslide dynamics. Geomorphology, 186(0), 12-27.

Sutton, M.A., Orteu, J.-J., Schreier, H.W., 2009. Image correlation for shape, motion and deformation measurements: basic concepts, theory and applications. Springer.

Teza, G., Galgaro, A., Zaltron, N., Genevois, R., 2007. Terrestrial laser scanner to detect landslide displacement fields: a new approach. International Journal of Remote Sensing, 28(16), 3425 - 3446.

Torralba, A., Oliva, A., 2003. Statistics of natural image categories. Network: Computation in Neural Systems, 14(3), 391-412.

Travelletti, J., 2011. Imagerie multi-paramètres et multi-résolutions pour l'observation et la caractérisation des mécanismes de glissements-coulées. PhD, Université de Caen Basse-Normandie, Strasbourg.

Travelletti, J., Delacourt, C., Allemand, P., Malet, J.P., Schmittbuhl, J., Toussaint, R., Bastard, M., 2012. Correlation of multi-temporal ground-based optical images for landslide monitoring: Application, potential and limitations. ISPRS Journal of Photogrammetry and Remote Sensing, 70(0), 39-55.

Travelletti, J., Malet, J.-P., Delacourt, C., 2014. Image-based correlation of Laser Scanning point cloud time series for landslide monitoring. International Journal of Applied Earth Observation and Geoinformation, 32.

Triggs, B., McLauchlan, P., Hartley, R., Fitzgibbon, A., 2000. Bundle Adjustment — A Modern Synthesis. In: B. Triggs, A. Zisserman, R. Szeliski (Eds.), Vision Algorithms: Theory and Practice. Lecture Notes in Computer Science. Springer Berlin Heidelberg, pp. 298-372.

Ullman, S., 1979. The interpretation of visual motion. MIT Press Series in Artificial Intelligence. MIT Press, Cambridge, Massachusetts, and London, England.

Ussyshkin, R.V., Smith, B., 2006. Performance analysis of ALTM 3100EA: Instrument specification and accuracy of LiDAR data. The International Archives of the Photogrammetry, Remote Sensing and Spatial Information Sciences,, 34, Part XXX.

Wenzel, K., Rothermel, M., Fritsch, D., Haala, N., 2013. Image Acquisition and model selection for multi-view stereo, 3D-ARCH 2013 - 3D Virtual Reconstruction and Visualization of Complex Architectures, Trento, Italy.

Westoby, M.J., Brasington, J., Glasser, N.F., Hambrey, M.J., Reynolds, J.M., 2012. 'Structure-from-Motion' photogrammetry: A low-cost, effective tool for geoscience applications. Geomorphology, 179(0), 300-314.

Wheaton, J.M., Brasington, J., Darby, S.E., Sear, D.A., 2010. Accounting for uncertainty in DEMs from repeat topographic surveys: improved sediment budgets. Earth Surface Processes and Landforms, 35(2), 136-156.

Whitehead, K., Moorman, B.J., Hugenholtz, C.H., 2013. Low-cost, on-demand aerial photogrammetry for glaciological measurement. The Cryosphere Discuss., 7(3), 3043-3057.

Wu, C., 2007. A GPU Implementation of Scale Invariant Feature Transform SIFT. http://cs.unc.edu/~ccwu/siftgpu, [last access: 31/10/2013].

Wu, C., 2013. Towards Linear-time Incremental Structure from Motion, International Conference on 3D Vision, University of Washington, Seattle, USA, pp. 8.

Wu, C., Agarwal, S., Curless, B., Seitz, S.M., 2011. Multicore bundle adjustment, Computer Vision and Pattern Recognition (CVPR), 2011 IEEE Conference on, pp. 3057-3064.

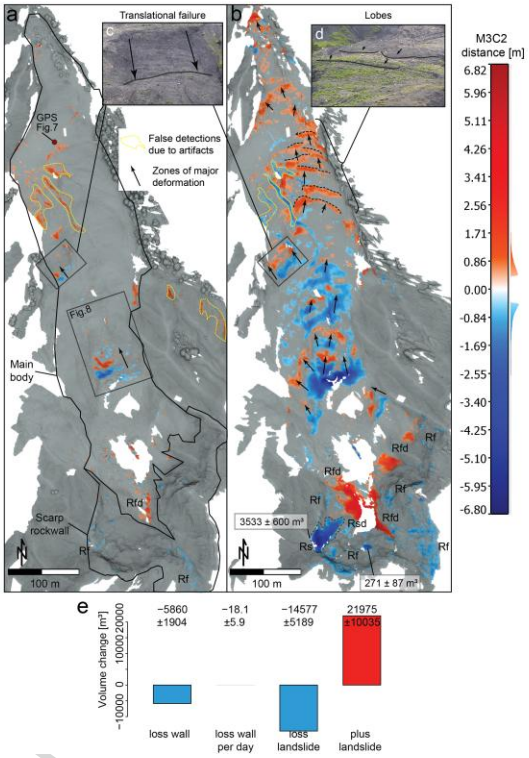

Graphical abstract